Remote Sensing of Environment 315 (2024) 114426

Contents lists available at ScienceDirect

Remote Sensing of Environment

journal homepage: www.elsevier.com/locate/rse

An analysis of the potentials of L-band SAR satellites for measuring azimuth motion

Cunren Liang [a,*], Eric J. Fielding [b], Zhen Liu [b], Takeshi Motohka [c], Ryo Natsuaki [d], Sang-Ho Yun [e,f,g]

[a] Institute of Remote Sensing and Geographic Information System, School of Earth and Space Sciences, Peking University, Beijing 100871, China
[b] Jet Propulsion Laboratory, California Institute of Technology, Pasadena, CA 91109, USA
[c] Earth Observation Research Center, Japan Aerospace Exploration Agency, 2-1-1 Sengen, Tsukuba-city, Ibaraki 305-8505, Japan
[d] Department of Electrical Engineering and Information Systems, The University of Tokyo, Tokyo 113-8656, Japan
[e] Earth Observatory of Singapore, Nanyang Technological University, Singapore 639798, Singapore
[f] Asian School of the Environment, Nanyang Technological University, Singapore 639798, Singapore
[g] School of Electrical and Electronic Engineering, Nanyang Technological University, Singapore 639798, Singapore

ARTICLE INFO

Editor: Jing M. Chen

Keywords:
Azimuth motion
InSAR
Ionosphere
L-band
MAI

ABSTRACT

Azimuth or along-track (approximately north-south) motion is critical in constructing three-dimensional ground motion with synthetic aperture radar (SAR) satellites orbiting the Earth in sun-synchronous polar orbit. The main problem of measuring azimuth motion with short-wavelength SAR data is decorrelation. A fleet of newly launched and upcoming long-wavelength L-band SAR satellites bring new opportunities for measuring azimuth motion. However, azimuth motion measured with L-band SAR data often contains large azimuth shifts caused by the Earth's ionosphere. We outline the framework of separating the azimuth motion and ionospheric azimuth shift from an analysis of the ionospheric effects on SAR images and SAR measurement precisions. We demonstrate three methods, among which one is newly proposed, can separate the azimuth motion and ionospheric azimuth shift with higher precisions. We evaluate the performances of the three methods by simulations using parameters of several selected L-band SAR satellites. The results show that, at kilometer resolutions, the azimuth motion measured by multiple-aperture SAR interferometry (MAI) can achieve centimeter precision, while the ionospheric azimuth shifts can be estimated with decimeter precision. Based on these results, a strategy for obtaining corrected azimuth motion is subsequently suggested, which achieves at least a first-order ionospheric correction of the original higher resolution MAI result. The three methods were also compared by real data processing examples. Furthermore, using real and simulated data of selected L-band SAR satellites, we present the first L-band MAI time series analysis result that measures subtle ground motion, as illustrated by the example of the postseismic deformation after the 2016 Kumamoto earthquakes in Japan. The performance is expected to be further improved with future L-band SAR missions that have much higher duty cycles. Some geophysical applications, in particular, those associated with the Earth's tectonic processes, can thus benefit from the azimuth motion measured by L-band SAR data.

1. Introduction

The three-dimensional ground motion vector can be completely represented by any three orthogonal vectors. However, under the imaging geometry of current spaceborne synthetic aperture radar (SAR) in sun-synchronous polar orbit, only one-dimensional measurement along Line-of-Sight (LOS) is made by interferometric SAR (InSAR). Two nearly orthogonal InSAR LOS measurements can be obtained by combining data of ascending and descending orbits, or left- and right-side looking directions. The missing component in completing the three-dimensional motion is thus the azimuth or along-track motion that is approximately in the north-south direction.

One of the trends of the technical development of SAR and InSAR is increasing the angular diversity to support three-dimensional observations as in Global Navigation Satellite System (GNSS). Some future missions are designed for this purpose, such as Harmony (López-Dekker et al., 2019) and CHORUS (Gondi et al., 2023) currently under development. Similar concepts as Harmony were also proposed for NISAR and

* Corresponding author.
E-mail address: cunren.liang@pku.edu.cn (C. Liang).

https://doi.org/10.1016/j.rse.2024.114426
Received 31 January 2024; Received in revised form 24 June 2024; Accepted 7 September 2024
0034-4257/© 2024 Elsevier Inc. All rights are reserved, including those for text and data mining, AI training, and similar technologies.

ROSE-L (Lavalle et al., 2023). However, most SAR missions, especially present ones, don't have such angular diversity. For these regular SAR missions, the azimuth angular diversity is limited by the SAR azimuth beamwidth. The azimuth beamwidth is split into a forward and a backward looks by multiple-aperture InSAR (MAI) to measure azimuth motion (Bechor and Zebker, 2006). Another method for measuring azimuth motion is cross correlation (Michel et al., 1999; Gray et al., 2000). Both MAI and cross correlation depend on coherence and are with much lower precisions compared with InSAR. MAI is efficient and easy to implement, and almost achieves Cramér-Rao Lower Bound (CRLB) (Bamler and Eineder, 2005). It is therefore preferred in practice. Compared with InSAR, the phase of the double-difference interferogram in MAI has stronger decorrelation noise. Furthermore, the noise is greatly amplified when converted to azimuth motion. Therefore, coherence is a major limiting factor in applying MAI with data acquired by SAR satellites operating at shorter wavelengths such as C-band.

Coherence is less of a problem for L-band SAR data. The pioneering spaceborne SAR missions including Seasat, SIR-A, SIR-B and SIR-C/X-SAR all worked at L-band, or at least carried an L-band radar. After that, however, the Japan Aerospace Exploration Agency (JAXA) had been the only space agency that operated L-band SAR satellites. Now we are entering the L-band age again. Three new L-band missions SAOCOM-1A/B, LuTan-1A/B and ALOS-4 are already in space. In the next few years, a fleet of L-band missions will launch including NISAR, ROSE-L and Tandem-L. The L-band SAR data from these missions can be exploited to measure azimuth motion.

As in InSAR, the troposphere and ionosphere are the main error sources in MAI as shown in Fig. 1. Sometimes there may also be residual error caused by the baseline difference between the two looks used in MAI (Jung et al., 2009). The troposphere is immediately above the ground and the lowest layer of the Earth's atmosphere. The height of the troposphere varies from about 7 to 8 km at the poles to about 16 to 18 km at the equator (Reichle, 2023). Thus its variation is small within the whole synthetic aperture or between the two looks in MAI. As the separation between the two looks becomes larger, however, the differential tropospheric delay between the two looks cannot be ignored. For the co-fliers mission concepts for NISAR and ROSE-L proposed in (Lavalle et al., 2023), troposphere should be considered. On the other hand, this higher sensitivity can be exploited to estimate tropospheric effect (Chen, 2004; Hensley et al., 2011). For present and near future L-band missions considered in this study, the separations between the two looks are not large, and therefore tropospheric effects are not significant.

Unlike troposphere, ionosphere extends from 50 km to 1000 km above the Earth's surface. The electrons in the ionosphere, which affect the propagation of electromagnetic waves, are normally with highest density at an altitude between 300 and 450 km. The linear component of the variations of the ionospheric total electron content (TEC) in azimuth imposes a linear phase on the azimuth radar phase history, and therefore leads to an azimuth shift in MAI and cross correlation results that is often too large to be ignored. Due to the ionospheric azimuth shift, L-band MAI time series analysis results are rarely seen in the literatures. In Wortham, 2014, MAI results with large ionospheric azimuth shifts are discarded before time series analysis. Some results of MAI time series analysis with ionospheric corrections were reported in (Liang et al., 2021; Liang et al., 2022). In (Mao et al., 2023), preliminary results are obtained.

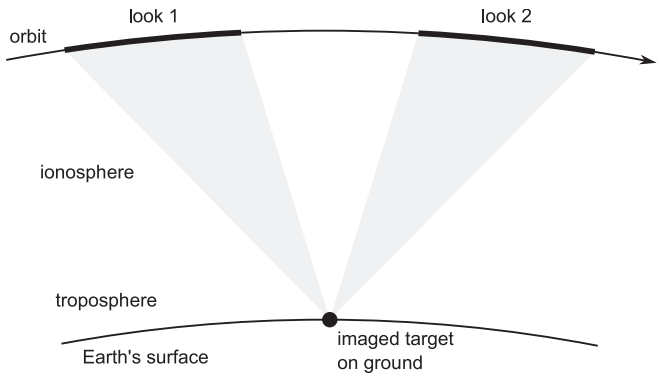

Fig. 1. The tropospheric and ionospheric effects in MAI.

In some cases, ionospheric azimuth shifts exhibit as "streaks" (Gray et al., 2000), that are spatially fast changing. Therefore, some researchers use a directional filter to remove them (Wegmüller et al., 2007; Raucoules and de Michele, 2010; Hu et al., 2012). In fact, spatially slow-changing shifts are more common (Liang et al., 2018), as can be seen from the results in Section 4. Instead of using a correction method that is based on the visual features of ionospheric azimuth shifts, the physical mechanism of ionospheric effects can be analyzed to develop a correction method. In particular, the dispersive nature of ionosphere has long been exploited in GNSS, and recently was successfully used to correct for InSAR ionospheric phase (Rosen et al., 2010; Brcic et al., 2010; Gomba et al., 2016). It is further used to correct for ionospheric azimuth shift (Liang and Fielding, 2017; Yamashita et al., 2022; Mao et al., 2022), but with lower precision. This dispersive nature can be used to correct for ionospheric azimuth shift.

In this paper, we evaluate the potentials of measuring azimuth motion with present and near future L-band SAR missions considering the ionospheric azimuth shift. To this end,

1) We outline the framework for measuring azimuth motion with L-band SAR data with a comprehensive analysis of the impacts of the ionosphere.
2) Among all possibilities under this framework, we demonstrate three methods are with higher precisions, with Method 3 as a newly proposed one.
3) We evaluate the performances of the three methods by simulations and real data examples for representative present and upcoming L-band SAR satellites. Based on simulation results, we propose the strategy to use high-resolution MAI processing with low-resolution ionospheric azimuth shift correction to obtain azimuth motions.
4) Using real and simulated data of representative present and upcoming L-band SAR satellites, we present the first L-band MAI time series analysis result that measures subtle ground motion, as illustrated by the example of the postseismic deformation after the 2016 Kumamoto earthquakes in Japan.

2. Separation of azimuth motion and ionospheric azimuth shift

2.1. The framework

Besides azimuth shift, ionosphere also causes other effects on SAR data. All these effects may be exploited, providing a number of possibilities for correcting for ionospheric azimuth shift. Here, we seek the best methods among the different possibilities.

To help understand the ionospheric effects on SAR data, we analyze and summarize them in Appendix A. The study of ionospheric effects on SAR has benefited from the experiences and practices of GNSS. Appendix A also helps to understand the common problems in SAR and GNSS that are caused by the ionosphere.

Appendix A summarizes four ionospheric effects represented by Eqs. (A.14) to (A.17). Other ionospheric effects, such as defocusing, are not considered here since they can hardly be modeled and used. For a pair of images used in InSAR, the four quantities become the differences between the two images accordingly. All four ionospheric effects depend on TEC, and vary with radar center frequency. This dispersive nature of the ionosphere can be exploited to separate the desired measurement and ΔTEC, which has been demonstrated in GNSS and recent advances in correcting for ionospheric effects in InSAR. ΔTEC measured by one quantity may also be used to mitigate the ionospheric effects in other quantities.

In range, the phase advance and range shift in Eqs. (A.14) and (A.15) are actually the same quantity with opposite signs if both are expressed in meters. This quantity can be measured by InSAR or cross correlation. Coherent cross correlation is more precise than incoherent cross correlation, and can achieve the CRLB (Bamler and Eineder, 2005). The approximate form of InSAR phase noise of a multiple-looked interferogram is given by (Rodriguez and Martin, 1992)

$$\sigma_{\phi_{\mathrm{InSAR}}} = \frac{1}{\sqrt{2N}} \frac{\sqrt{1-\gamma^2}}{\gamma} \tag{1}$$

where γ is the coherence, and N is the number of resolution elements. N should be large enough to make Eq. (1) valid. The precision achieved by coherent cross correlation in resolution elements is given by (Bamler, 2000)

$$\sigma_{\mathrm{cc}} = \sqrt{\frac{3}{2N}} \frac{\sqrt{1-\gamma^2}}{\pi\gamma} \tag{2}$$

The precision ratio of InSAR and coherent cross correlation measurements is thus

$$r_{\mathrm{insar-cc}} = \frac{\frac{\lambda}{4\pi}\sigma_{\phi_{\mathrm{InSAR}}}}{\rho_r \sigma_{\mathrm{cc}}} = \frac{\lambda}{4\sqrt{3}\rho_r} \tag{3}$$

where ρ_r is the range resolution. Eq. (3) shows that $r_{\mathrm{insar-cc}}$ is much smaller than 1 for current SAR systems, and therefore InSAR is better in precision than coherent cross correlation as demonstrated in practice.

In azimuth, the azimuth shift in Eq. (A.16) can be measured by MAI or cross correlation. MAI is less precise than, but very close to coherent cross correlation. MAI is more precise than incoherent cross correlation (Bamler and Eineder, 2005). Considering the difficulties in implementing coherent cross correlation, e.g., removing the phase pattern in the matching window, and its efficiency, MAI is still superior in estimating azimuth shift.

The last ionospheric effect that can be exploited is the Faraday rotation in Eq. (A.17). However, Faraday rotation loses sensitivity to TEC near equator where ionospheric effect is strongest, as it depends on the angle between the Earth's magnetic field and the electromagnetic wave propagation θ (Wright et al., 2003; Le Vine and Abraham, 2002). Besides, estimating Faraday rotation requires fully polarimetric data (Freeman, 2004; Rogers and Quegan, 2014). The estimation is subject to system distortions, such as crosstalk and channel imbalance (Quegan and Lomas, 2015). Present and upcoming satellite L-band SAR systems either don't have the capability of acquiring fully polarimetric data, or have limited quota for fully polarimetric data in their data acquisition plans. Therefore, estimating ΔTEC from Faraday rotation effect is not a good candidate for our purpose.

To conclude, phase measurements implemented by InSAR or MAI are better suited for estimating ΔTEC. The phase arising from ΔTEC is the dispersive component of the measurements. The measurements also contain ground motions and other components that do not depend on radar frequency, and therefore are not dispersive. As in GNSS, multiple frequency measurements can be made to estimate ΔTEC and ground motion by making use of the dispersive nature of ionosphere. Specifically, three possible methods can be considered

- **Method 1:** Perform MAI processing. Estimate the ionospheric azimuth shift using ΔTEC or ionospheric phase estimated by the dispersive nature in InSAR processing, and remove it from the MAI result.
- **Method 2:** Perform MAI processing. Estimate the ionospheric azimuth shift using the dispersive nature in MAI, and remove it from the MAI result.
- **Method 3:** Use the dispersive nature in MAI to directly obtain the ionospheric-free azimuth motion directly.

2.2. Implementation of the methods

Following the already established conventions, we call the two subbands backward and forward looks in azimuth, and lower and upper bands in range.

In InSAR, the non-dispersive phase is caused by the range differences between the two acquisitions as a result of topography $\Delta r_{\mathrm{topography}}$, troposphere $\Delta r_{\mathrm{troposphere}}$ and ground motion $\Delta r_{\mathrm{motion}}$, while the dispersive component is caused by the difference in the total electron content along radar LOS ΔTEC in the ionosphere

$$\begin{aligned}\phi_{\mathrm{InSAR}} &= \phi_{\mathrm{InSAR,non-disp}} + \phi_{\mathrm{InSAR,ion}} \\ &= \frac{4\pi f_0}{c}\left(\Delta r_{\mathrm{topography}} + \Delta r_{\mathrm{troposphere}} + \Delta r_{\mathrm{motion}}\right) - \frac{4\pi K_2}{c f_0}\Delta\mathrm{TEC}\end{aligned} \tag{4}$$

If converted to distance by multiplying by $c/4\pi f_0$, (4) is given by

$$\frac{c}{4\pi f_0}\phi_{\mathrm{InSAR}} = \Delta r = \left(\Delta r_{\mathrm{topography}} + \Delta r_{\mathrm{troposphere}} + \Delta r_{\mathrm{motion}}\right) - \frac{K_2}{f_0^2}\Delta\mathrm{TEC} \tag{5}$$

Using the dispersive nature of the ionosphere as in GPS, the range split-spectrum method (Rosen et al., 2010; Brcic et al., 2010; Gomba et al., 2016; Liang and Fielding, 2017), or dual-frequency/wavelength method, uses two different wavelengths or center frequencies to estimate the phase contribution from ionosphere. In this method, a SAR image has two copies including a lower and an upper band images, each with a different center frequency. Currently, the lower and upper band images are generated by bandpass filtering the full range spectrum of a SAR image. Some operation modes of future L-band SAR systems, such as NISAR and ALOS-4, are designed to have a main and a side bands, and therefore naturally acquire two images of different center frequencies simultaneously. The InSAR phases of the lower and upper band images can be derived from Eq. (4)

$$\begin{cases}\phi_{\mathrm{InSAR},l} = \frac{f_l}{f_0}\phi_{\mathrm{InSAR,non-disp}} + \frac{f_0}{f_l}\phi_{\mathrm{InSAR,ion}} \\ \phi_{\mathrm{InSAR},u} = \frac{f_u}{f_0}\phi_{\mathrm{InSAR,non-disp}} + \frac{f_0}{f_u}\phi_{\mathrm{InSAR,ion}}\end{cases} \tag{6}$$

where f_l and f_u are the center frequencies of the lower and upper bands. The non-dispersive and dispersive components of the InSAR phase are then given by (Rosen et al., 2010; Brcic et al., 2010; Gomba et al., 2016; Liang and Fielding, 2017)

$$\begin{cases}\phi_{\mathrm{InSAR,non-disp}} = \frac{f_0}{f_u^2 - f_l^2}\left(f_u\phi_{\mathrm{InSAR},u} - \phi_l f_{\mathrm{InSAR},l}\right) \\ \phi_{\mathrm{InSAR,ion}} = \frac{f_l f_u}{f_0\left(f_u^2 - f_l^2\right)}\left(f_u\phi_{\mathrm{InSAR},l} - f_l\phi_{\mathrm{InSAR},u}\right).\end{cases} \tag{7}$$

Multiplying by $c/4\pi f_0$ gives the results in distance units

$$\begin{cases}\frac{c}{4\pi f_0}\phi_{\mathrm{InSAR,non-disp}} = \Delta r_{\mathrm{non-disp}} = \frac{c}{4\pi\left(f_u^2 - f_l^2\right)}\left(f_u\phi_{\mathrm{InSAR},u} - \phi_l f_{\mathrm{InSAR},l}\right) \\ \frac{c}{4\pi f_0}\phi_{\mathrm{InSAR,ion}} = \Delta r_{\mathrm{ion}} = \frac{c f_l f_u}{4\pi f_0^2\left(f_u^2 - f_l^2\right)}\left(f_u\phi_{\mathrm{InSAR},l} - f_l\phi_{\mathrm{InSAR},u}\right).\end{cases} \tag{8}$$

In (Wegmüller et al., 2018), Eq. (7) was reformulated to make the method more robust.

The estimated ionospheric phase can be used to estimated the azimuth shift introduced by ionosphere in MAI (Liang and Fielding, 2017). By using Eqs. (A.11) and (A.12), the result is

$$\Delta a_{\mathrm{ion}} = \frac{v_g}{4\pi K_a}\frac{\partial\Delta\phi_{\mathrm{InSAR,ion}}}{\partial\eta} = \frac{\lambda R_0 v_g}{8\pi v_r^2 \cos^3\theta_{r,c}}\frac{\partial\Delta\phi_{\mathrm{InSAR,ion}}}{\partial\eta} \tag{9}$$

In multiple-aperture InSAR (MAI), the non-dispersive component is caused by azimuth ground motion, while the dispersive component is

caused by the difference of the linear change of total electron content along radar LOS within the synthetic aperture between the two acquisitions ΔTEC. Here we have neglected the tropospheric and orbit differences (Jung et al., 2009) between the two azimuth looks, which is also non-dispersive. The basic MAI equation for measuring azimuth motion Δa_{motion} is given by (Liang and Fielding, 2017)

$$\phi_{\text{MAI}} = -\frac{2\pi\left(f_{\text{DC},f} - f_{\text{DC},b}\right)}{v_g}\Delta a_{\text{motion}} \tag{10}$$

Considering also the dispersive component

$$\phi_{\text{MAI}} = \phi_{\text{MAI,non-disp}} + \phi_{\text{MAI,ion}} = -\frac{2\pi\left(f_{\text{DC},f} - f_{\text{DC},b}\right)}{v_g}\left(\Delta a_{\text{motion}} + \Delta a_{\text{ion}}\right) \tag{11}$$

where $f_{\text{DC},f}$ and $f_{\text{DC},b}$ are the Doppler centroid frequencies of the forward and backward looks, and Δa_{ion} is the difference of the azimuth shifts caused by ionosphere between the two acquisitions.

Δa_{ion} is given by Eq. (A.16). Hence, Eq. (11) can be written as

$$\begin{aligned}\phi_{\text{MAI}} &= \phi_{\text{MAI,non-disp}} + \phi_{\text{MAI,ion}} \\ &= -\frac{2\pi\left(f_{\text{DC},f} - f_{\text{DC},b}\right)}{v_g}\Delta a_{\text{motion}} + \frac{1}{f_0^2}\cdot\frac{\pi\left(f_{\text{DC},f} - f_{\text{DC},b}\right)R_0}{v_r^2 cos^3\theta_{r,c}}\cdot K_2\cdot\frac{\partial\Delta\text{TEC}}{\partial\eta}\end{aligned} \tag{12}$$

Multiplying by $-v_g/2\pi\left(f_{\text{DC},f} - f_{\text{DC},b}\right)$ gives the result in distance units

$$-\frac{v_g}{2\pi\left(f_{\text{DC},f} - f_{\text{DC},b}\right)}\phi_{\text{MAI}} = \Delta a = \Delta a_{\text{motion}} - \frac{1}{f_0^2}\cdot\frac{R_0 v_g}{2v_r^2 cos^3\theta_{r,c}}\cdot K_2\cdot\frac{\partial\Delta\text{TEC}}{\partial\eta} \tag{13}$$

This result is similar, in form, to Eq. (5). The main difference is that phase and distance conversion depends on f_0 in InSAR, but does not in MAI. This results in some differences in the final solutions for non-dispersive and dispersive phases between MAI and InSAR.

As in InSAR, the non-dispersive component and dispersive component can also be estimated by the dual-frequency method, e.g. Mao et al., 2022. Then the lower band and upper band images are created and their MAI phases are

$$\begin{cases}\phi_{\text{MAI},l} = \phi_{\text{MAI,non-disp}} + \dfrac{f_0^2}{f_l^2}\phi_{\text{MAI,ion}} \\ \phi_{\text{MAI},u} = \phi_{\text{MAI,non-disp}} + \dfrac{f_0^2}{f_u^2}\phi_{\text{MAI,ion}}\end{cases} \tag{14}$$

Inverting Eq. (14), the non-dispersive and dispersive phases are obtained

$$\begin{cases}\phi_{\text{MAI,non-disp}} = \dfrac{f_l^2\phi_{\text{MAI},l} - f_u^2\phi_{\text{MAI},u}}{f_l^2 - f_u^2} \\ \phi_{\text{MAI,ion}} = \dfrac{f_u^2 f_l^2}{f_0^2\left(f_l^2 - f_u^2\right)}\left(\phi_{\text{MAI},u} - \phi_{\text{MAI},l}\right)\end{cases} \tag{15}$$

In distance units, the corresponding azimuth motion and ionospheric shift difference between the two acquisitions are

$$\begin{cases}\Delta a_{\text{motion}} = -\dfrac{v_g}{2\pi\left(f_{\text{DC},f} - f_{\text{DC},b}\right)}\dfrac{f_l^2\phi_{\text{MAI},l} - f_u^2\phi_{\text{MAI},u}}{f_l^2 - f_u^2} \\ \Delta a_{\text{ion}} = -\dfrac{v_g}{2\pi\left(f_{\text{DC},f} - f_{\text{DC},b}\right)}\dfrac{f_u^2 f_l^2}{f_0^2\left(f_l^2 - f_u^2\right)}\left(\phi_{\text{MAI},u} - \phi_{\text{MAI},l}\right)\end{cases} \tag{16}$$

From these analyses, the three methods for obtaining an ionospheric-free MAI result can be implemented as follows

- **Method 1:** Perform MAI processing using Eq. (11). Estimate the ionospheric azimuth shift using ionospheric phase estimated in InSAR processing as in Eq. (9), and remove it from the MAI result.
- **Method 2:** Perform MAI processing using Eq. (11). Estimate the ionospheric azimuth shift using lower and upper band MAI results as in the second equation of Eq. (16), and remove it from the MAI result.
- **Method 3:** Use lower and upper band MAI results to compute azimuth motion directly as in the first equation of Eq. (16).

As in the ionospheric phase estimation in InSAR shown in Eqs. (7) and (8), the results in Eq. (16) are very noisy. Directly computing azimuth motion using the first equation of Eq. (16) would lose the fine details in the MAI results. The workflows of the three methods are presented in Fig. 2.

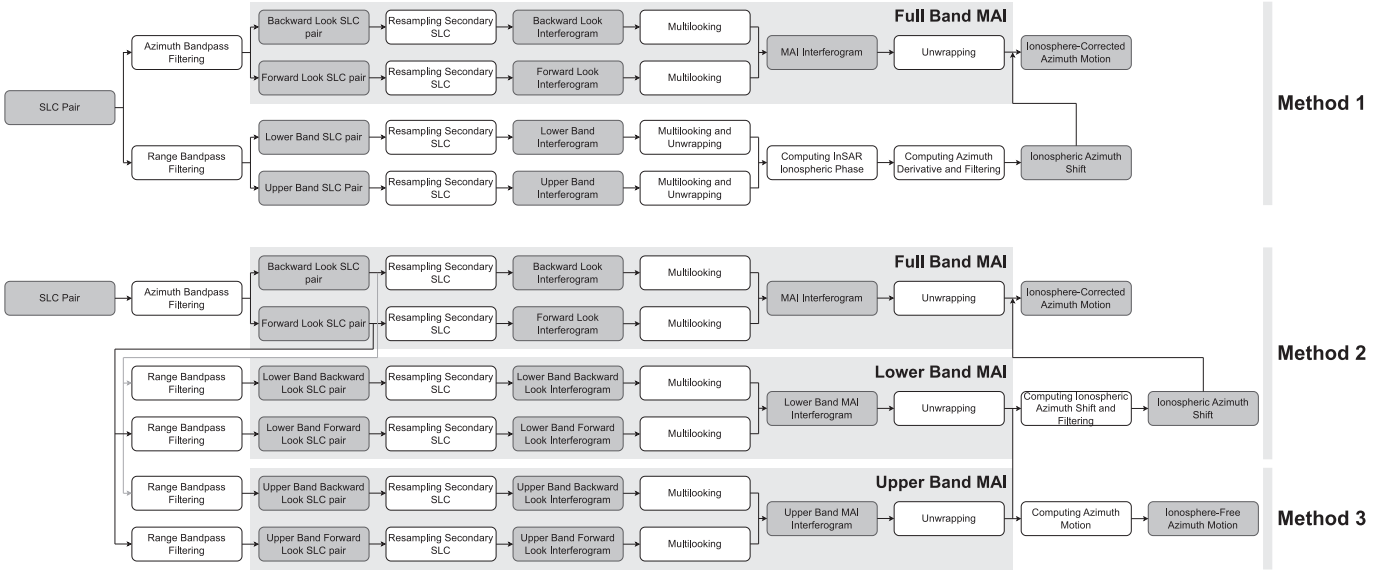

Fig. 2. The workflows of the three methods for measuring azimuth motion. For operation modes with a side band such as ALOS-4 28 + 10 MHz mode, azimuth bandpass filtering is applied to the main band (and the side band for methods 2 and 3), and the range bandpass filtering is no longer required. In this case, the full band MAI result is either the lower or upper band MAI result. In Methods 2 and 3, the order of range and azimuth bandpass filtering can be switched, or they can be combined as a 2-D bandpass filtering.

2.3. Precision of the methods

The forward and backward looks in MAI are independent, since the azimuth spectra of the two looks do not overlap. The standard deviation of MAI phase is then

$$\sigma_{\phi_{\mathrm{MAI}}} = \sqrt{\sigma_{\phi_f}^2 + \sigma_{\phi_b}^2} \tag{17}$$

where σ_{ϕ_f} and σ_{ϕ_b} are the phase standard deviation of the forward and backward looks, respectively, and can be given by Eq. (1). The precision of the MAI measurement is

$$\sigma_{\Delta a_{\mathrm{motion}}} = \frac{v_g}{2\pi\left(f_{\mathrm{DC},f} - f_{\mathrm{DC},b}\right)}\sigma_{\phi_{\mathrm{MAI}}} \tag{18}$$

In InSAR, the lower and upper band interferograms used to estimate ionospheric phase are also independent. According to Eq. (7), the standard deviation of the estimated ionospheric phase is then

$$\sigma_{\phi_{\mathrm{InSAR,ion}}} = \frac{f_l f_u}{f_0\left(f_u^2 - f_l^2\right)}\sqrt{f_u^2\sigma_{\phi_l}^2 + f_l^2\sigma_{\phi_u}^2} \tag{19}$$

Using Eq. (9), the standard deviation of the estimated ionospheric azimuth shift is

$$\sigma_{\Delta a_{\mathrm{ion}}} = \frac{v_g}{4\pi K_a}\frac{\sqrt{\sigma_{\phi_{\mathrm{InSAR,ion},i+1}}^2 + \sigma_{\phi_{\mathrm{InSAR,ion},i}}^2}}{\Delta\eta} \tag{20}$$

where $\sigma_{\phi_{\mathrm{InSAR,ion},i}}$ and $\sigma_{\phi_{\mathrm{InSAR,ion},i+1}}$ are the standard deviations of the two pixels used to compute the derivative in discrete form.

In the dual-frequency method for MAI, the standard deviations of the estimated azimuth motion and ionospheric azimuth shift difference can be derived using Eq. (16)

$$\begin{cases} \sigma_{\Delta a_{\mathrm{motion}}} = -\dfrac{v_g}{2\pi\left(f_{\mathrm{DC},f} - f_{\mathrm{DC},b}\right)}\dfrac{1}{f_l^2 - f_u^2}\sqrt{f_l^4\sigma_{\phi_{\mathrm{MAI},l}}^2 + f_u^4\sigma_{\phi_{\mathrm{MAI},u}}^2} \\ \sigma_{\Delta a_{\mathrm{ion}}} = -\dfrac{v_g}{2\pi\left(f_{\mathrm{DC},f} - f_{\mathrm{DC},b}\right)}\dfrac{f_u^2 f_l^2}{f_0^2\left(f_l^2 - f_u^2\right)}\sqrt{\sigma_{\phi_{\mathrm{MAI},u}}^2 + \sigma_{\phi_{\mathrm{MAI},l}}^2} \end{cases} \tag{21}$$

where $\sigma_{\phi_{\mathrm{MAI},l}}$ and $\sigma_{\phi_{\mathrm{MAI},u}}$ are the phase standard deviations of the lower and upper band MAI interferograms, respectively.

In the above analysis, note that f_0 becomes the center frequency of the main range band, either f_l or f_u, for operation modes with a side band as mentioned in the later sections.

2.4. Time series analysis

Time series analysis techniques can be used to track the temporal evolution of the azimuth motions. The time series analysis techniques established in regular InSAR processing can be employed, but different options are available.

For Methods 1 and 2, the time series analysis can be performed separately for azimuth motion and ionospheric azimuth shift, leading to time series of azimuth motion and ionospheric azimuth shift. Alternatively, the pair-wise ionospheric azimuth shift can be removed from the pair-wise azimuth motion first, and then the time series analysis can be performed on the corrected azimuth motions. A more advanced option would be the joint time series analysis of both azimuth motion and ionospheric azimuth shift. For Method 3, time series can be performed directly on the ionospheric-free azimuth motions.

In any option, an error model for the time series analysis is helpful in suppressing the noise level of the resulting time series, considering the fact that the random noises in the measurements are much larger than those in InSAR measurements. Spatial filtering can also be used to suppress the random noises in the azimuth motion and ionospheric azimuth shift. Stronger filtering may be applied to ionospheric azimuth shift as it has lower precision compared to azimuth motion as shown in Sections 2.3 and 3. Note that the strong filtering of ionospheric azimuth shift does not cause the loss of the fine details of the azimuth motion measurements. Further study can investigate whether the spatial filtering should be carried out before or after the time series analysis.

3. Evaluation of the precision of azimuth measurements of selected L-band missions

3.1. Overview of spaceborne L-band SAR missions

Spaceborne L-band SAR missions started from the first civil Earth observing SAR satellite Seasat launched in 1978. Subsequent Shuttle Imaging Radar (SIR) series all carry L-band SAR instruments including SIR-A in 1981, SIR-B in 1984, and two SIR-C/X-SAR missions in 1994. Since 1992, continuous L-band SAR satellite observations were made by JAXA's L-band missions including JERS-1 (1992–1998), ALOS (2006–2011) and ALOS-2 (2014–).

Over the years, X-band and C-band comprise the main sources of SAR data. Now L-band missions are growing rapidly. Three new missions are already in space including the Argentine space agency CONAE's SAOCOM-1A and SAOCOM-1B launched on October 8, 2018 and August 30, 2020, the Chinese bistatic L-band SAR satellites LuTan-1A and LuTan-1B launched on January 26, and February 27, 2022, and JAXA's ALOS-4 launched on July 1, 2024. Looking ahead, the NASA-ISRO NISAR mission is planned to launch in the near future. Other future L-band SAR satellite missions include European Space Agency (ESA)'s ROSE-L and German Aerospace Center (DLR)'s Tandem-L. With these missions, we are entering the golden age of L-band SAR.

Early L-band spaceborne SAR missions operated in the basic single polarization stripmap mode. ScanSAR and spotlight modes, as well as quad-pol mode, were then demonstrated by SIR-C/X-SAR (Freeman et al., 2019). Following L-band SAR satellites including ALOS, ALOS-2, SAOCOM and LuTan-1 all have the capability to operate in ScanSAR or TOPS mode to cover wide swaths with lower azimuth resolutions, but still mainly operate in the stripmap mode except ALOS-2 that uses ScanSAR mode as its default operation mode. ROSE-L is designed to operate in one-look ScanSAR mode, but recently a two-look ScanSAR mode was proposed that can benefit azimuth motion measurement (Perna et al., 2024). Next generation L-band SAR satellites, such as NISAR, employ digital beamforming (DBF), sometimes along with reflector antennas, to provide stripmap-like images with both high resolution and wide swath.

3.2. Precision of azimuth measurements of selected L-band missions

The noises in both azimuth motion and ionospheric measurements are strong. High-resolution SAR data are helpful in suppressing the noises, in which case a larger number of looks can be applied. In addition, frequent data acquisition is required for systematic and long-term motion measurement. Therefore, we evaluate the performance of some selected operation modes from current and upcoming SAR satellites. The parameters of these operation modes are shown in Table 1. Some of these operation modes have a wide swath, e.g. the NISAR 20 + 5 MHz mode. Since the time window for receiving the echo is long to cover the wide swath, and the same antenna should also be used to transmit signal, there are gaps in the radar echoes. By dithering the PRF, known as staggered SAR (Villano et al., 2014), the gaps can be distributed over the scene. Its impact on InSAR is not significant (Zebker, 2021) and is not considered here. The three stripmap modes of ALOS-2 and ALOS-4 have similar system parameters, except that ALOS-4 can image wide swaths by using DBF, and has a side band for ionospheric correction in its 28 + 10 MHz mode. Therefore, the ALOS-2 84 MHz and ALOS-4 42 MHz modes in Table 1 can represent the corresponding acquisition modes of both ALOS-2 and ALOS-4. LuTan-1 has five stripmap modes, one

Table 1
System parameters of selected operation modes of current and upcoming L-band SAR satellites analyzed in this study. Note that range and azimuth resolutions are resolutions on ground and computed using parameters that can vary depending on satellite positions, incidence angles etc. Range resolution variations due to varying incidence angle may be significant. Range resolution is computed at an incidence angle of 40 degrees, which is also used in the simulation. ALOS-4 azimuth bandwidths are from the corresponding ALOS-2 modes. The azimuth bandwidth and azimuth resolution are approximated values for LuTan-1.

Mode	ALOS-2 84 MHz	ALOS-4 28 + 10 MHz	ALOS-4 42 MHz	LuTan-1 80 MHz	NISAR 20 + 5 MHz	NISAR 40 + 5 MHz
Altitude [km]	~628	~628	~628	~607	~740	~740
Revisit Time [days]	14	14	14	4	12	12
Center Frequency [MHz]	1257.50	1236.50/1294.50	1236.50	1260.00	1229.00/1293.50	1239.00/1293.50
Wavelength [cm]	23.84	24.25/23.16	24.25	23.79	24.39/23.18	24.20/23.18
Operation Mode	Stripmap	Stripmap	Stripmap	Stripmap	SweepSAR	SweepSAR
Swath Width [km]	50	200	100/200	50	240	240
Range Bandwidth [MHz]	79.40	28 + 10 (total: 77)	42	80.00	20 + 5 (total: 77)	40 + 5 (total: 77)
Azimuth Bandwidth [Hz]	2395.48	1355.93	1671.27	2395.48	1100.00	1100.00
Range Resolution [m]	~2.94	~8.33/23.32	~5.55	~2.91	~11.66/46.64	~5.83/46.64
Azimuth Resolution [m]	~2.89	~5.10	~4.14	~2.88	~6.09	~6.09

ScanSAR modes and three experimental modes, among which one stripmap mode called Strip 1 was recently selected to systematically acquire data. Thus Strip 1 mode is evaluated in this paper. The Strip 1 mode can image different swaths by changing antenna elevation angles. The average processed azimuth bandwidth of different elevation angles is close to that of ALOS-2 84 MHz mode. Considering their range bandwidths are also the same, the performances of ALOS-2 84 MHz mode and LuTan-1 should be the same, and therefore we use one result to represent both ALOS-2 84 MHz mode and LuTan-1 in the following evaluations.

The standard deviations of azimuth motion and ionospheric azimuth shift are computed at kilometer resolutions in order to get usable results. The standard deviations of the azimuth motion computed using Eq. (18) for different operation modes are shown in Fig. 3. These results show that centimeter precision can be achieved if there is only random noise due to decorrelation in the MAI interferograms. The standard deviations of the ionospheric azimuth shift computed using Eq. (20) in Method 1 for different operation modes are shown in Fig. 4. Their counterparts computed using Eq. (21) in Method 2 are shown in Fig. 5. The two results do not differ much, both achieving decimeter precision. For higher resolution and lower coherence results, Method 2 is more precise. On the other extreme, Method 1 is better. Fig. 6 shows the standard deviations of the azimuth motion, free of ionosphere, computed using Eq. (21) in Method 3 for different operation modes. These results are very close to those in Fig. 5.

As a general conclusion, at kilometer resolutions, the azimuth motion measured by MAI can achieve centimeter precision, while the ionospheric azimuth shifts, as well as the ionospheric-free azimuth motion estimated by Method 3, can be estimated with decimeter precision.

3.3. A processing strategy for methods 1 and 2

For Methods 1 and 2, the standard deviations show that, at same

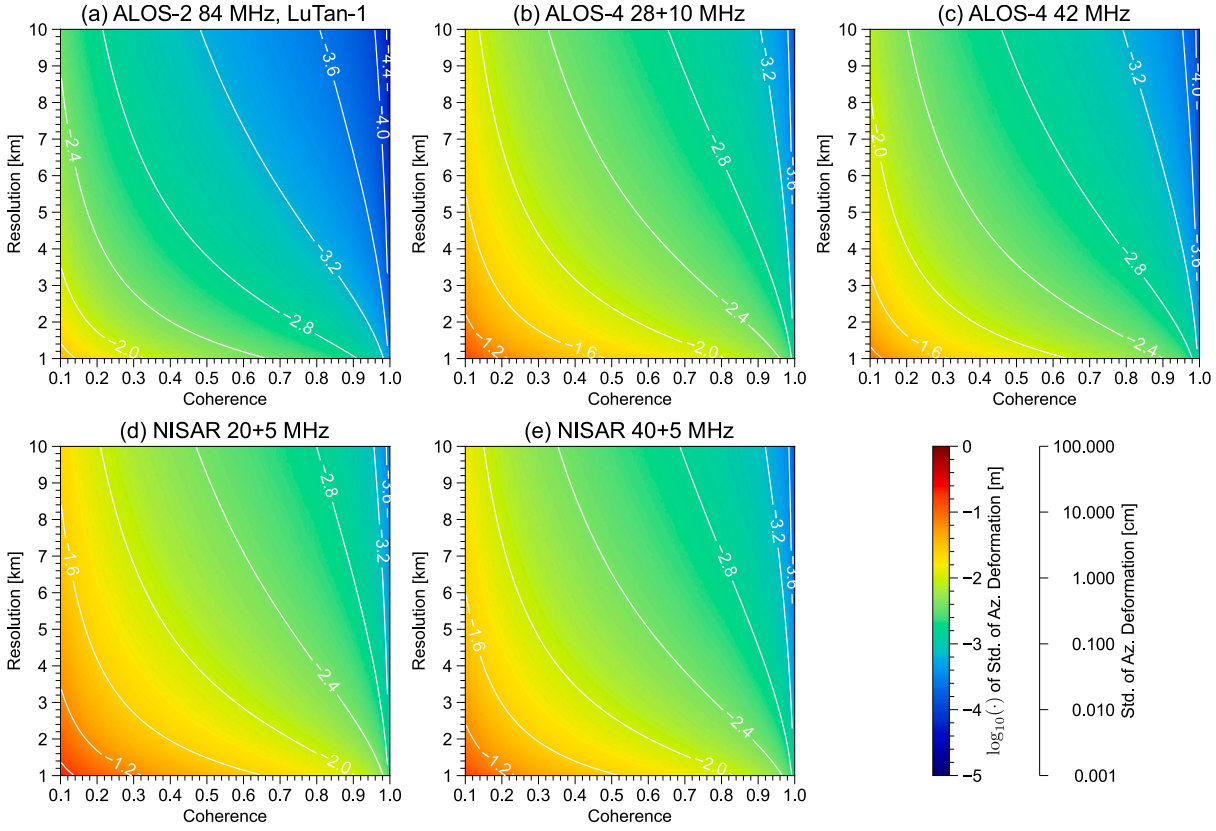

Fig. 3. The standard deviations of the azimuth motion computed using MAI for different operation modes.

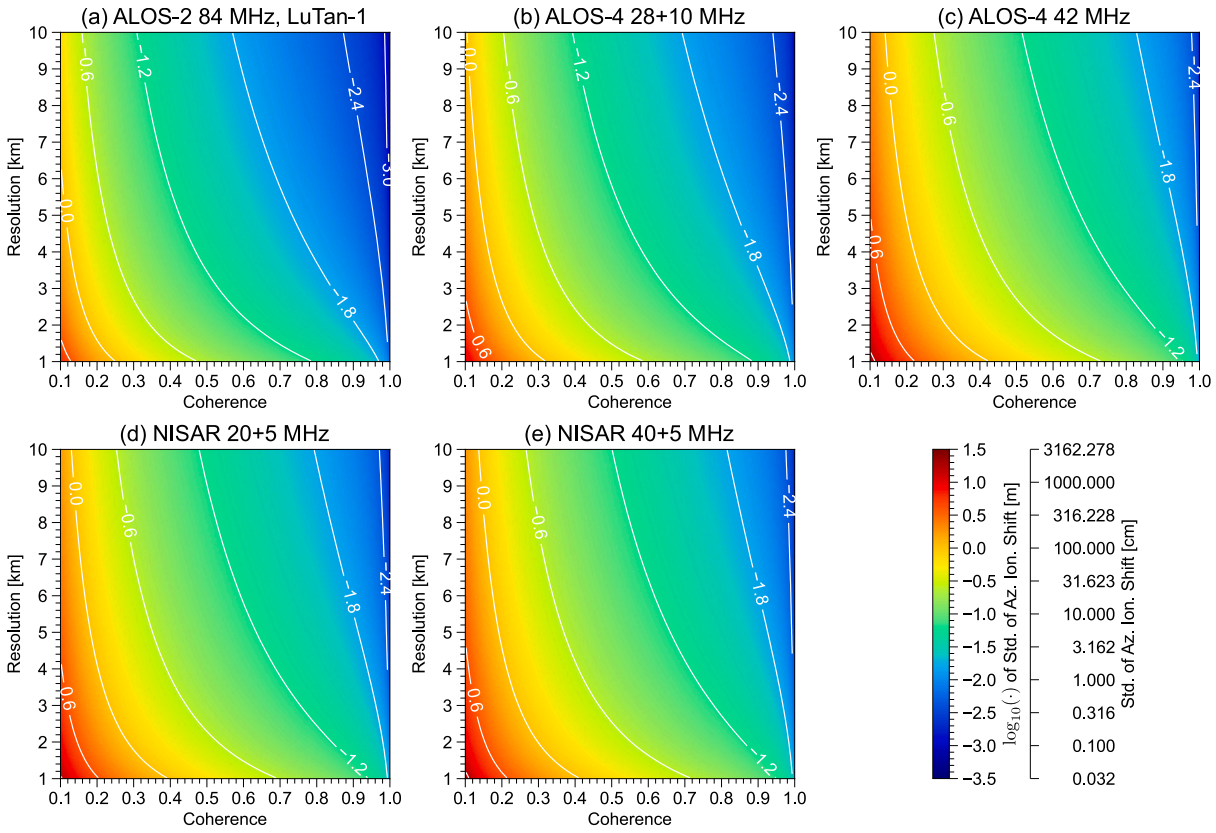

Fig. 4. The standard deviations of the ionospheric azimuth shift computed using Method 1 for different operation modes.

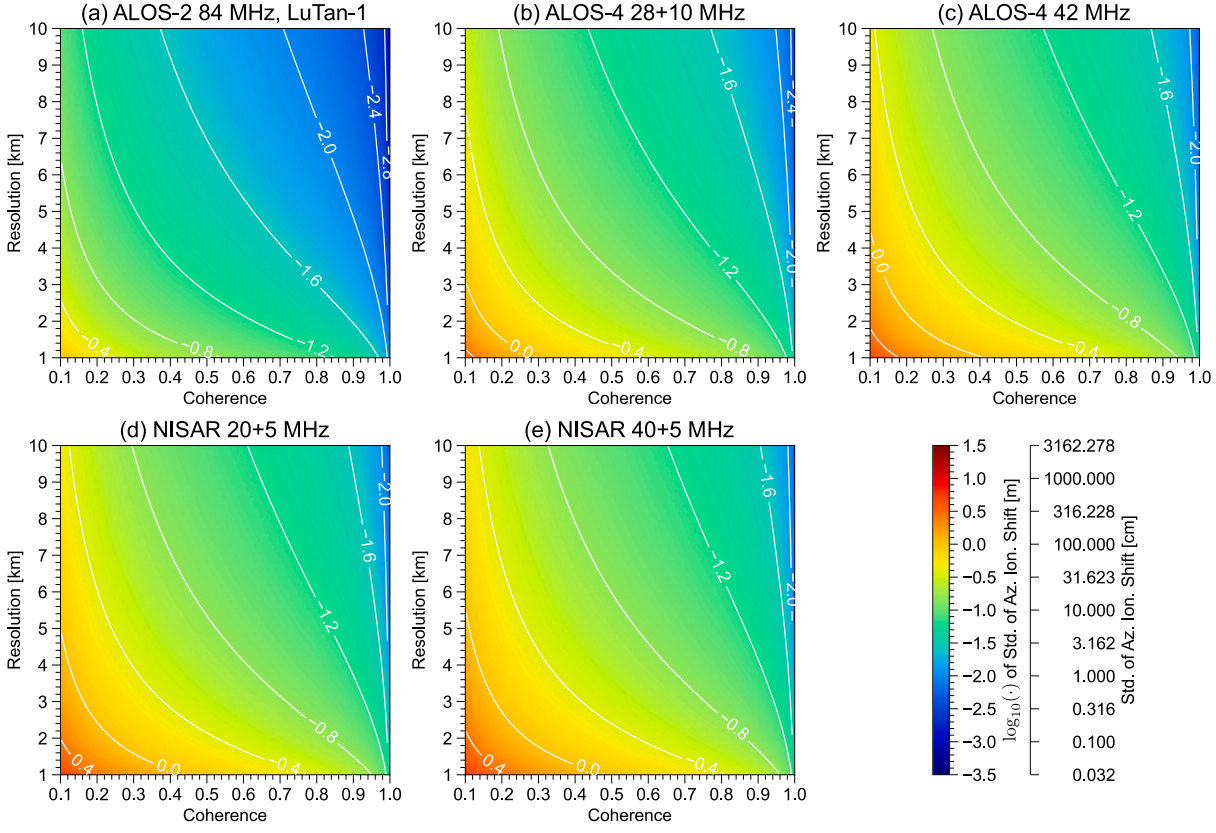

Fig. 5. The standard deviations of the ionospheric azimuth shift computed using Method 2 for different operation modes.

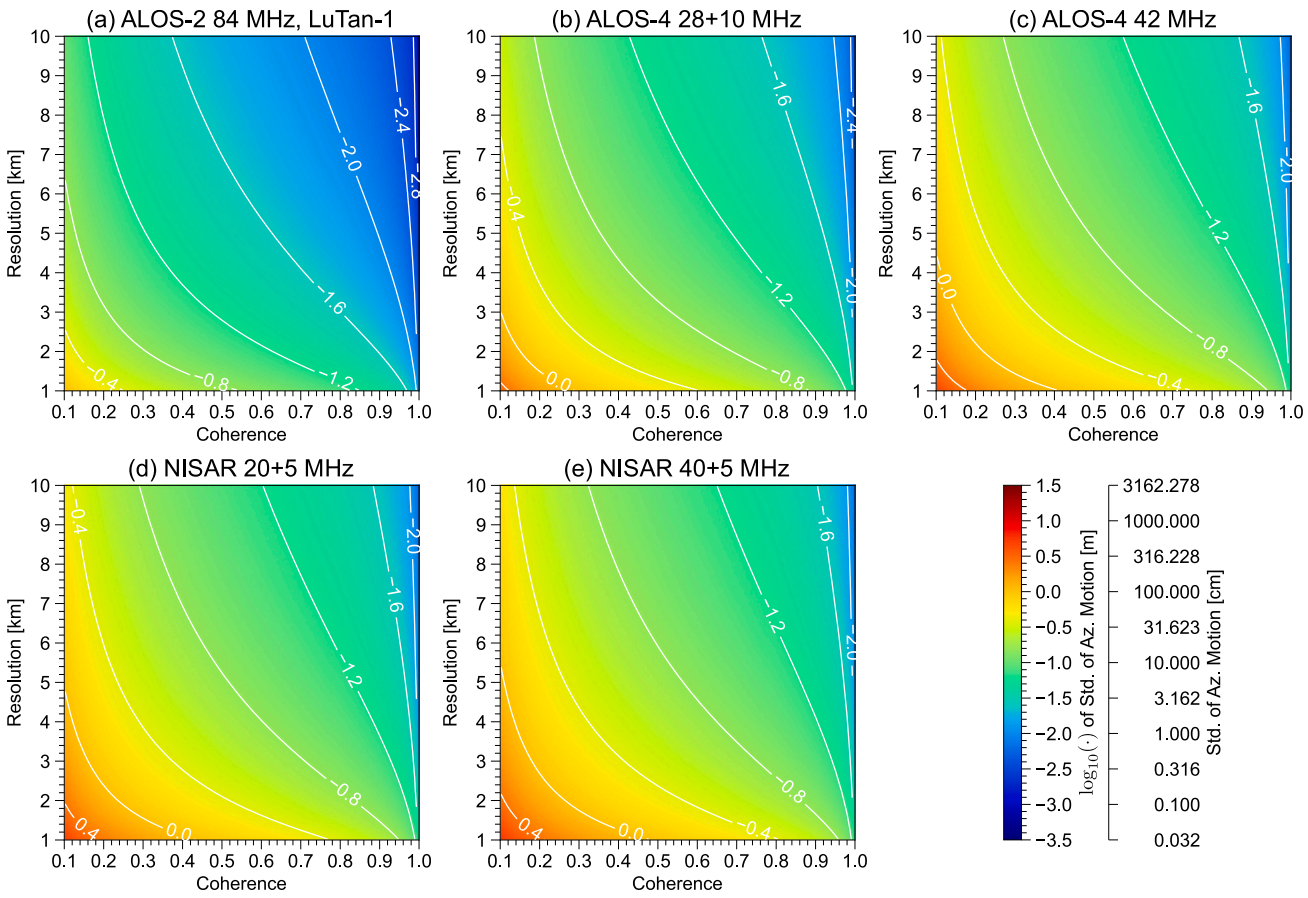

Fig. 6. The standard deviations of the azimuth motion, free of ionosphere, computed using Method 3 for different operation modes.

resolutions, the estimated ionospheric azimuth shifts are with lower precisions compare with azimuth motion measured by MAI. In real data processing, a smaller number of looks can be applied to azimuth motion to retain fine motion details. On the other hand, the ionospheric azimuth shift can be processed with a larger number of looks or strongly filtered in order to match the precision of azimuth motion. This results in a first-order lower-resolution ionospheric correction. As a result, spatially fast-changing components of the ionospheric azimuth shift cannot be corrected as shown in Section 4.

Note that correcting high-resolution InSAR measurements with low-resolution data is also a fact in tropospheric correction. In corrections with global atmospheric models, the mostly used ERA-5 data have a spatial resolution of 0.25° or about 27.6 km at equator.

4. Demonstration of azimuth motion measurement capability with real data

Sections 2 and 3 provide theoretical and simulation results of measuring measuring azimuth motion with selected L-band SAR satellites. In this section, we demonstrate azimuth motion measurement capability with real data acquired by ALOS-2, as well as data of other selected L-band missions simulated using ALOS-2 data.

4.1. Data

The frequency band from 1215 to 1300 MHz is allocated for L-band spaceborne active sensors operating in the Earth exploration-satellite (active) and space research (active) services by the International Telecommunications Union (https://www.itu.int/dms_pubrec/itu-r/rec/rs/R-REC-RS.577-7-200902-I!!PDF-E.pdf). Additional national restrictions may also apply, making the available frequency band even smaller (Spencer and Ulaby, 2016) as shown in Table 1. Currently, the most abundant L-band satellite SAR data are acquired by JAXA's ALOS-2 satellite. Its ultra-fine stripmap mode has a range bandwidth of 79.40 MHz (nominal bandwidth 84 MHz) as shown in Table 1. It spans almost the entire frequency band allocated for L-band spaceborne SAR. It also has a very large azimuth bandwidth. While it is not the default operation mode of ALOS-2, many data were acquired in Japan. These characteristics make it an ideal candidate for carrying out experiments and simulating data of other missions, considering there are not yet enough data acquired by other missions for time series analysis.

The ALOS-2 data used in this study cover the 2016 Kumamoto earthquakes in Japan including an Mw 6.2 foreshock and an Mw 6.0 foreshock on April 14 and an Mw 7.0 mainshock on April 15 (UTC). A total of 43 images were acquired on descending track 23 at local time 12:18 PM from September 7, 2015 to March 2, 2020. Two frames including 2950 and 2960 are processed to cover the whole deformation area. To simulate data of other operation modes or satellites, the ALOS-2 84 MHz data are bandpass filtered in both range and azimuth to get the range and azimuth bands of these modes or satellites. This also applies to the side band, if any. Fig. 7 shows an example of simulating NISAR 20 + 5 MHz data. Note that there is an artifact in the range spectrum of the data, likely due to the removal of Radio Frequency Interference (RFI) before or in the focusing of the data. Therefore, the positions of the main and side bands of the NISAR 20 + 5 MHz mode are switched in order to avoid its impacts.

4.2. Processing

The SLCs of the two frames are first mosaicked, which requires the offsets between the two frames. The offsets cannot be computed using near range and azimuth starting time of the data because sometimes

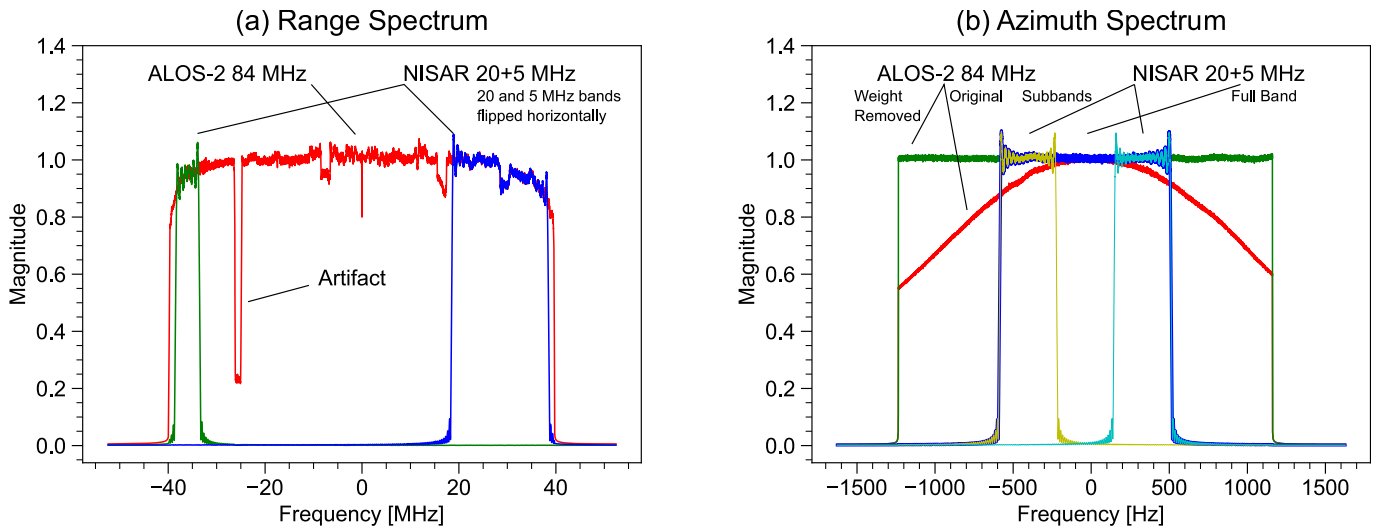

Fig. 7. Spectra of ALOS-2 84 MHz and NISAR 20 + 5 MHz modes. ALOS-2 data acquired on April 18, 2016 are used to compute the spectra. (a) Range spectrum. (b) Azimuth spectrum. Note that for range spectrum, we have switched the positions of the main and side bands of the NISAR 20 + 5 MHz mode to avoid the impact of the artifact in the original ALOS-2 84 MHz range spectrum, that is likely caused by the removal of radio frequency interference. Note also that weighting is not applied in the NISAR 20 + 5 MHz spectra.

they are not precise enough. Instead, the offsets between the two frames are estimated by cross correlation with data of the overlap area. These are the same data but focused in different frames. Theoretically the coherence between the overlap-area data of different frames is 1, and there is no error in the estimated offsets since cross correlation depends on coherence. The second frame is then resampled to align with the first one. The phase difference between the two frames is also removed.

After the SLCs are mosaicked, we follow the workflows in Fig. 2 for the rest of the processing. The mosaicked ALOS-2 SLCs are filtered in azimuth and/or in range, depending on the operation mode in Table 1, to get the range and azimuth subband images required to implement the methods introduced in Section 2. For operation modes with a side band such as ALOS-4 28 + 10 MHz mode, azimuth bandpass filtering is applied to the main band (and the side band for methods 2 and 3), and the range bandpass filtering is no longer required. In this case, the full band MAI result is either the lower or upper band MAI result. If a band of an operation mode is to be split in either range or azimuth direction, it is evenly divided by three as this scheme achieves CRLB (Bamler and Eineder, 2005). This is repeated for each acquisition mode in Table 1. To coregister the SLCs, the geometric offsets are first computed between each secondary date and reference date April 18, 2016. The secondary SLCs are resampled using the geometric offsets. Then, in each direction, a residual constant offset is estimated between the reference SLC and each resampled secondary SLC using cross correlation. Finally, each secondary SLC is resampled using both geometric offsets and the residual constant offsets to match the reference SLC.

The decorrelation is very strong in this area, with a mean coherence of only 0.22. For the MAI processing in the three methods shown in Fig. 2, we use a smaller number of looks and filter the multilooked interferograms, instead of using a large number of looks. The number of looks is 64 × 96 (range × azimuth), resulting a pixel size of 142.42 × 204.73 m^2 on the ground. In full band MAI processing shown in Fig. 2, MAI interferograms are filtered by the Goldstein-Werner filter (Goldstein and Werner, 1998) with a filter strength 1.0, a window size 128 and a step size 32. The MAI interferograms are unwrapped by the statistical-cost network-flow algorithm (Chen and Zebker, 2001). In Method 2, the computed ionospheric azimuth shift is filtered by an iterative Gaussian filter.

For the dual-frequency method shown in the lower part of Method 1 in Fig. 2 (Rosen et al., 2010; Brcic et al., 2010; Gomba et al., 2016), the data are processed with same number of looks as in MAI processing. In using Eq. (9) to compute ionospheric azimuth shift, a larger azimuth time interval $\partial\eta$ would lead to a more precise result, but with lower resolution. We use an interval of 40 lines, ~8.2 km on the ground. Note that the azimuth resolution of the estimated ionospheric phase is the same as SAR aperture length. Due to the antenna pattern, the actual azimuth resolution is a little smaller than radar aperture length. The interval is thus not a large value since it is much smaller than the aperture length, which is about 28.9 km on the ground for the ALOS-2 84 MHz mode in Table 1. The computed ionospheric azimuth shift is then filtered by the same iterative Gaussian filter used in Method 2.

4.3. Single pair results

In Methods 1 and 2, the resolution of the computed ionospheric azimuth shift is only a little smaller than aperture length. Moreover, the computed ionospheric azimuth shift is spatially filtered. Therefore, it cannot be used to remove ionospheric azimuth shift that is spatially fast-changing. Fortunately, in most cases, ionospheric azimuth shift is slow-changing as opposed to the streaks. Using Method 1, Fig. 8 shows an example of successful correction result for a pair of ALOS-2 84 MHz acquisitions. The corrected MAI result reveals a deformation pattern that is consistent with that of InSAR interferogram shown in Fig. 8 (d). Also using Method 1, the ionospheric azimuth shift is not well removed for the case shown in Fig. 9, since there are fast-changing components that cannot be removed by the method.

Figure 10 compares the azimuth deformations of the same event measured by the three methods using the same data as in Fig. 8. The results of Methods 1 and 2 are almost the same. Clearly, Methods 1 and 2 are superior by making use of the strategy that computes high-resolution MAI and corrects it with low-resolution ionospheric azimuth shift. In this case, the true ionospheric azimuth shift is slow-changing, and therefore this trick works. With Method 3, however, we are only able to get a low-resolution MAI result regardless of the spatial changing rate of the ionospheric azimuth shift.

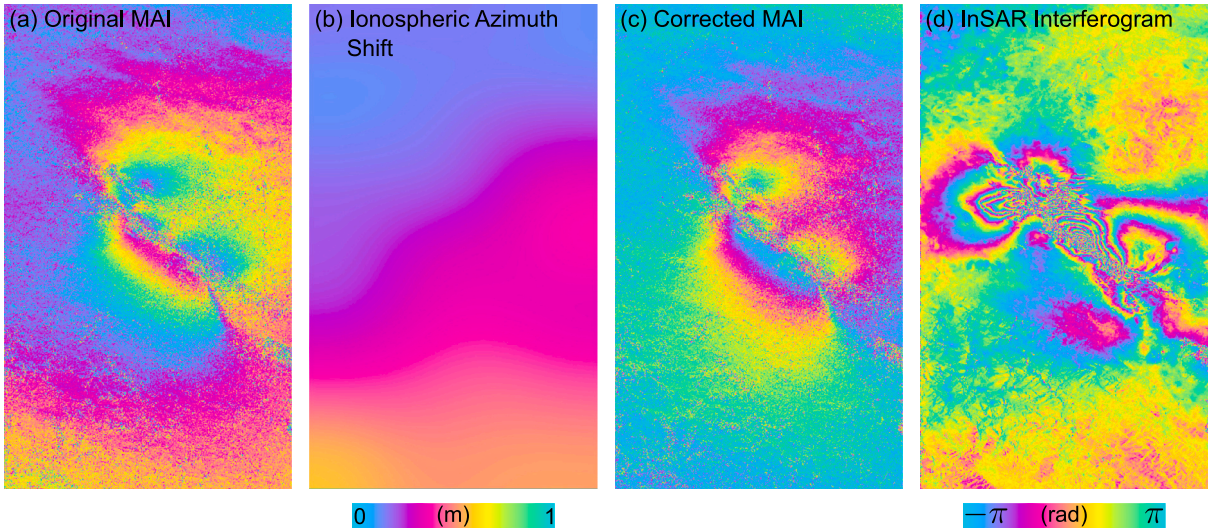

Fig. 8. Correcting MAI result for ionospheric azimuth shift by Method 1. The data were acquired in ALOS-2 84 MHz mode on March 7 and April 18, 2016, respectively. The ionospheric azimuth shift is largely removed since it's spatially slow-changing. The MAI interferograms are not filtered in the processing.

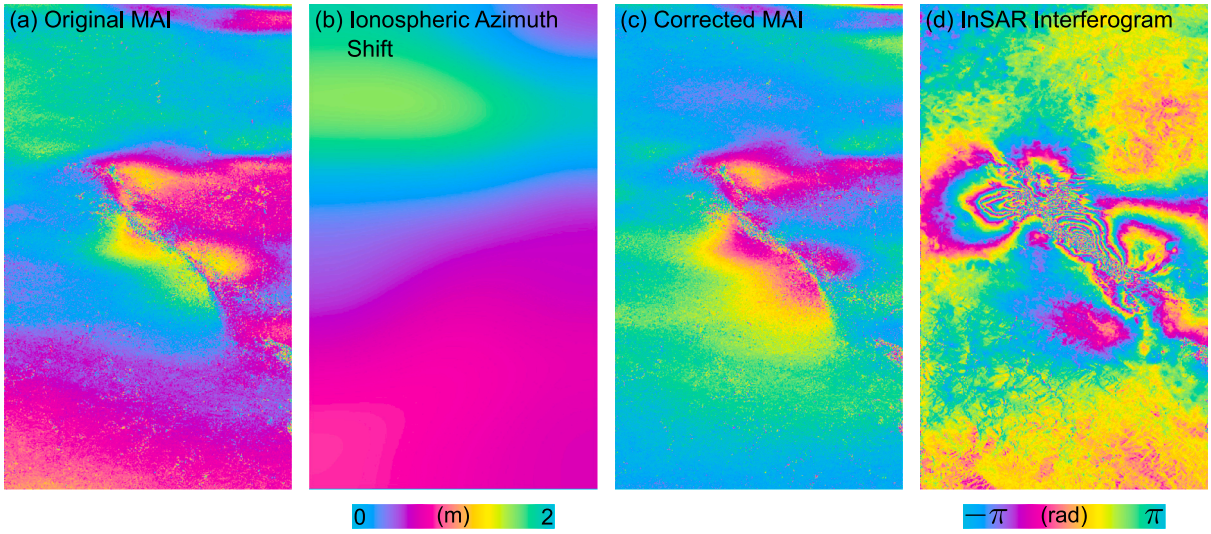

Fig. 9. Correcting MAI result for ionospheric azimuth shift by Method 1. The data were acquired in ALOS-2 84 MHz mode on March 7 and May 2, 2016, respectively. The ionospheric azimuth shift is not well removed since there are spatially fast-changing components in it. The MAI interferograms are not filtered in the processing.

4.4. Time series results

By using Methods 1 and 2 and the strategy in Section 3.3, we can get a high-resolution MAI result with a first-order ionospheric azimuth shift correction. In addition, as the results of Methods 1 and 2 are almost the same as examined in Section 4.3, here we present the results processed by Method 1.

We aim to measure the small postseismic deformation after the 2016 Kumamoto earthquakes using the post-earthquake acquisitions. Among the acquisitions, those containing spatially fast-changing ionospheric azimuth shifts are discarded, leaving 32 acquisitions from April 18, 2016 to March 2, 2020. These remaining acquisitions are used to form all 496 MAI pairs, among which 64 bad pairs are discarded. For each pair, we perform both MAI processing and ionospheric azimuth shift processing. The estimated ionospheric azimuth shift is then removed from the MAI result. Finally, we perform a simple least-squares estimation of azimuth deformations of individual dates using the corrected MAI results, and estimate a linear deformation rate.

Figure 11 shows the individual MAI correction results. The pairs are formed between reference date April 18, 2016 and each secondary date. After the correction, the postseismic deformation, along with the possible secular deformation, gradually show up in the individual MAI results as the time span increases. The deformation pattern is similar to that of coseismic deformation shown in Fig. 8.

Geocoded postseimic deformation velocity from MAI time series analysis for ALOS-2 84 MHz mode is shown in Fig. 12. The original MAI velocity field is strongly affected by spatially slow-changing ionosphere. After correction, it agrees with GPS velocities. Although both postseismic and secular deformations contribute to the velocity, postseismic deformation should be the main cause. Therefore, the velocity field is clearly delineated by the coseismic surface rupture, and agrees with the coseismic InSAR interferogram. However, we also observe clear discrepancies between the MAI and GPS results in the area inside the dashed circle. The difference is correlated with the topography of this area. We are not sure of the cause. We doubt it might be related to troposphere, or residual topographic contribution (Jung et al., 2009). We currently don't have an effective method to remove it.

Results of other satellites are shown in Figs. 13–16. These results are

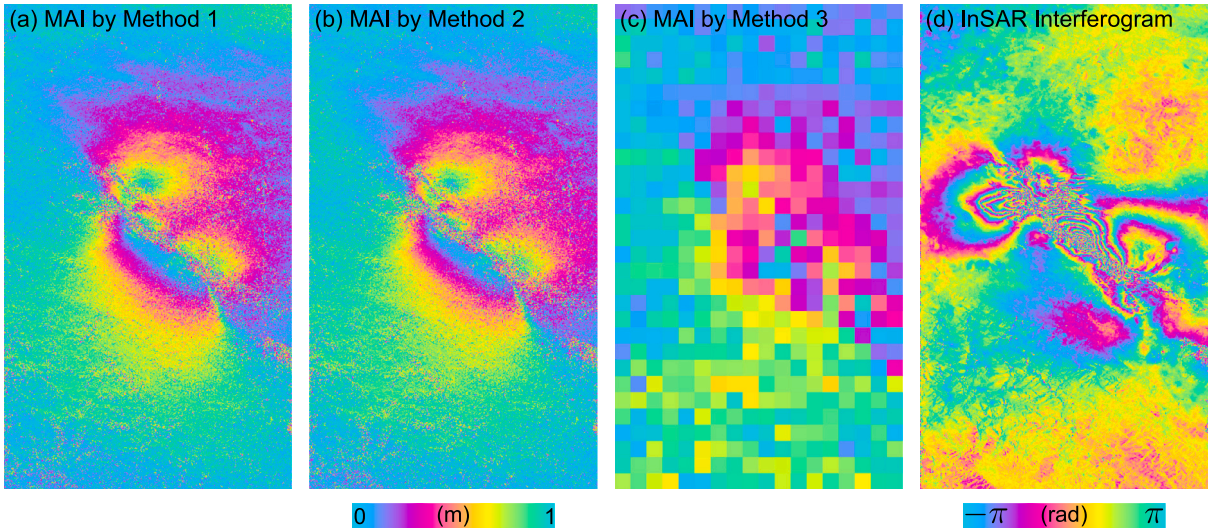

Fig. 10. MAI results computed by different methods, with ionospheric azimuth shift corrected or free of ionospheric azimuth shift. The data used are the same as those in Fig. 8. The MAI interferograms are not filtered in the processing.

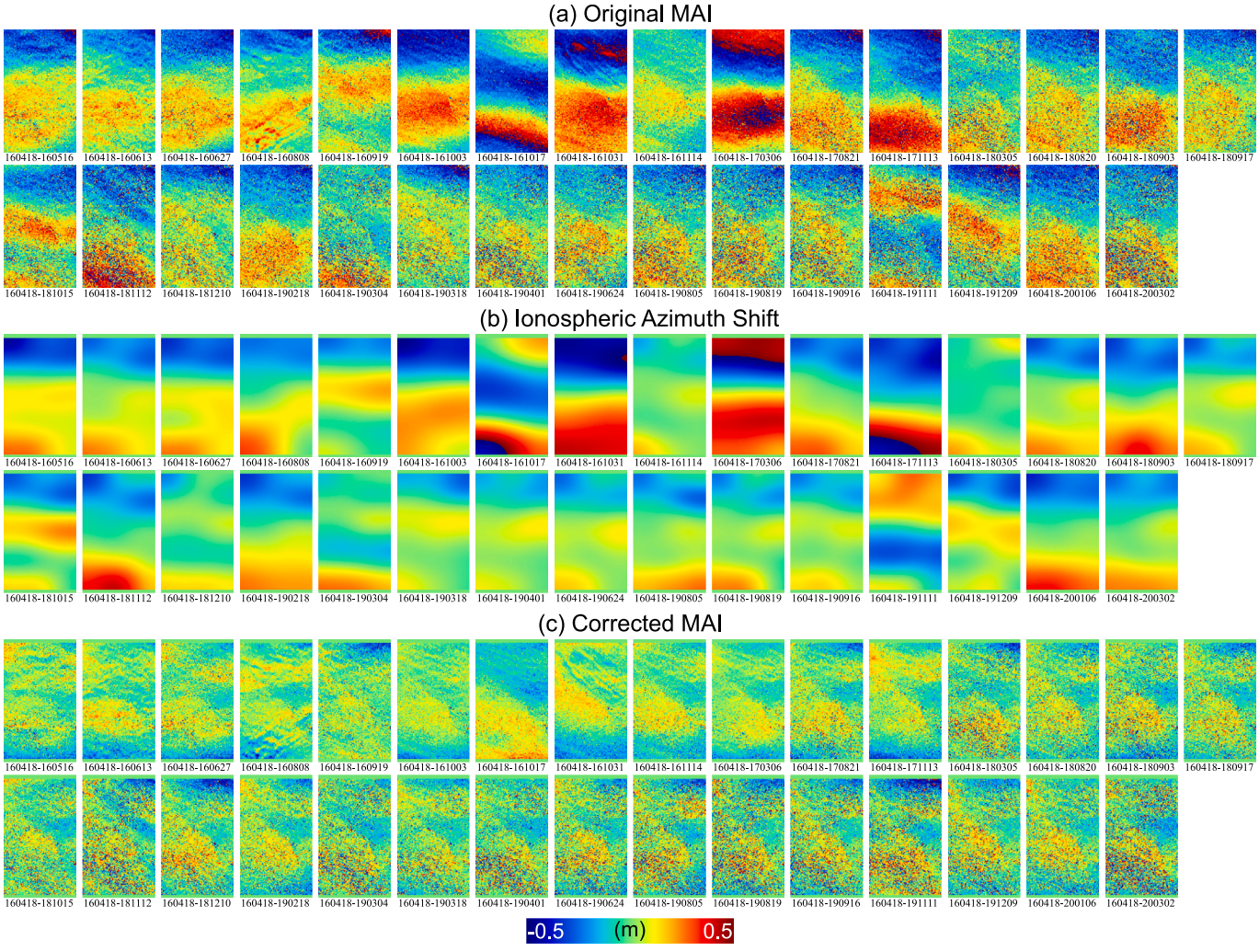

Fig. 11. Correcting for ionospheric azimuth shift in individual MAI results. (a) Original MAI. (b) Ionospheric azimuth shift. (c) Corrected MAI. As the time span increases, the postseismic and secular deformations show up in the corrected MAI results, which are in agreement with the coseismic deformation shown in Fig. 7.

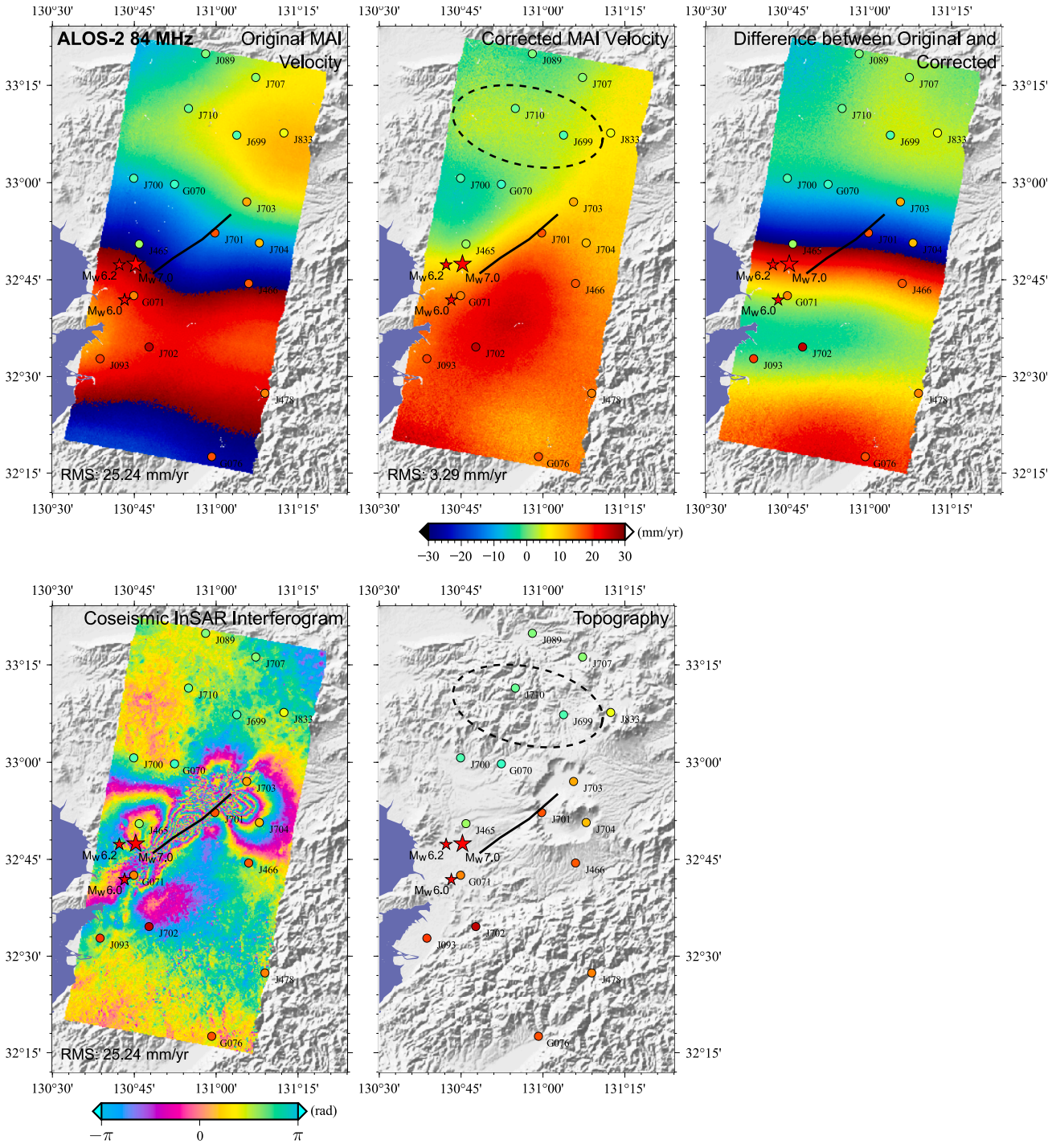

Fig. 12. Azimuth deformation velocity after the 2016 Kumamoto earthquakes in Japan from MAI time series analysis with ALOS-2 84 MHz data. GPS stations are represented by circles. The colors inside the circles represent the GPS velocities projected into radar azimuth directions. The thick line in each panel is surface rupture identified from the InSAR coseismic interferogram. The stars denote the epicenters of the foreshocks and mainshock. This result also represents that of LunTan-1 since the key system parameters are nearly the same for the two satellites.

processed with exactly the same parameters. Some have much higher noise level due to lower resolution and thus fewer number of looks available in multiple looking, but all results agree with GPS measurements.

In Fig. 17, we further present the deformation time series, measured by ALOS-2 84 MHz data used in Fig. 12, at GPS Station J466 referenced to Station J707. Results from other stations and measured by other datasets are similar. The result is still not precise enough to track the temporal evolution of the deformation. However, there is still possibility to do this in high coherence areas with temporally dense data from future missions, such as NISAR.

4.5. Discussion

The mean coherence of the area in the case study is only 0.22. Because of this, stronger filtering is required to get a usable result. Most areas would have a coherence higher than this area. Therefore, the filtering strength can be relaxed, and the result is expected to be better.

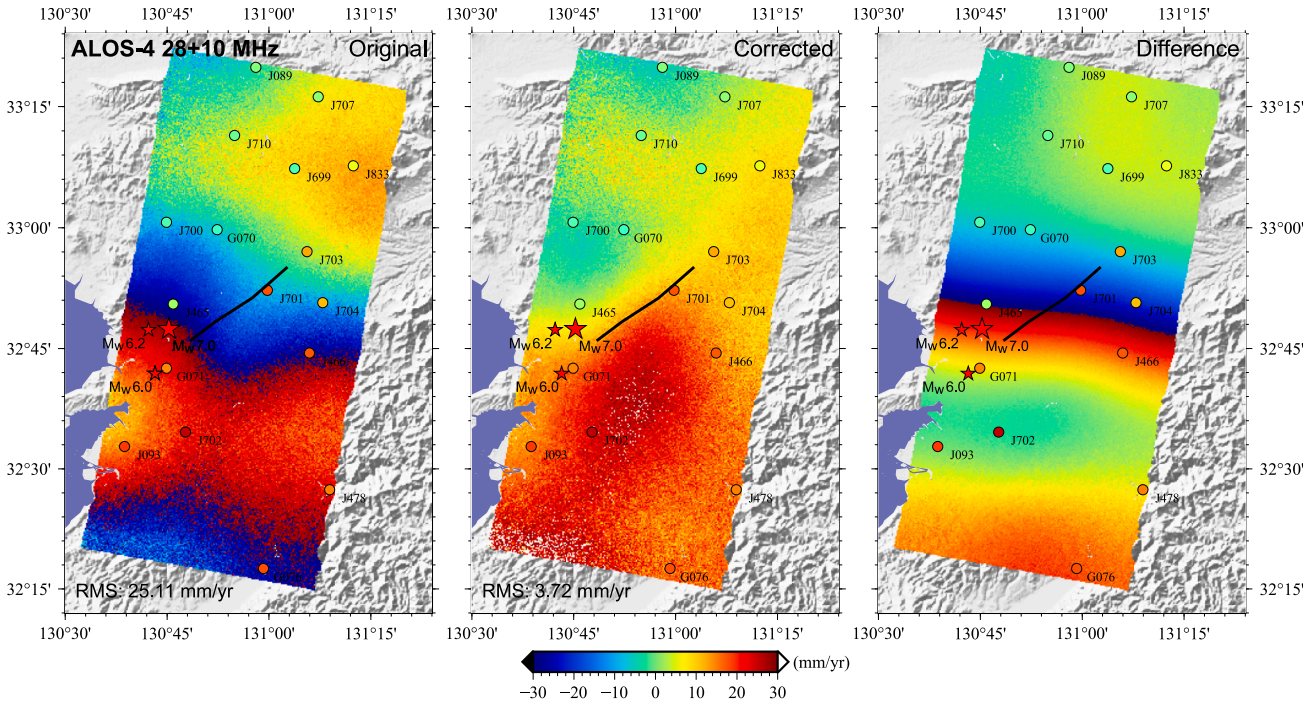

Fig. 13. Azimuth deformation velocity after the 2016 Kumamoto earthquakes in Japan from MAI time series analysis with simulated ALOS-4 28 + 10 MHz data. GPS stations are represented by circles. The colors inside the circles represent the GPS velocities projected into radar azimuth directions. The thick line in each panel is surface rupture identified from the InSAR coseismic interferogram. The stars denote the epicenters of the foreshocks and mainshock.

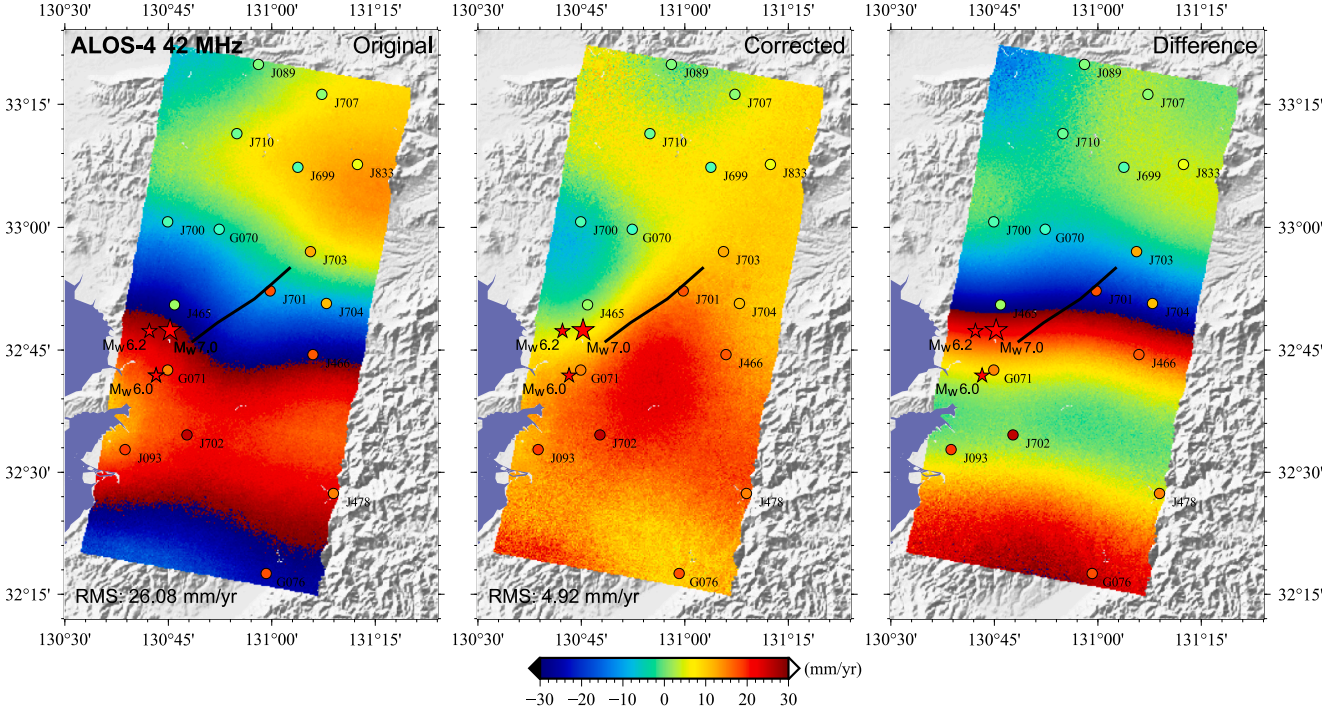

Fig. 14. Azimuth deformation velocity after the 2016 Kumamoto earthquakes in Japan from MAI time series analysis with simulated ALOS-4 42 MHz data. GPS stations are represented by circles. The colors inside the circles represent the GPS velocities projected into radar azimuth directions. The thick line in each panel is surface rupture identified from the InSAR coseismic interferogram. The stars denote the epicenters of the foreshocks and mainshock.

The average acquisition frequency of the data is about 39 days per acquisition. The performance of some of the future missions would be much better. For example, NISAR has a revisit time of 12 days. The average duty cycle of the NISAR L-band radar is at least 50 %, enabling it to acquire data every time it passes a land area. The results shown in Figs. 15 and 16 would be greatly improved with real NISAR data. Combining data from both ascending and descending tracks will further double the acquisition frequency and improve the MAI time series. Another potential improvement is using both NISAR's L-band and S-band data to obtain a more precise ionospheric azimuth shift estimate. In

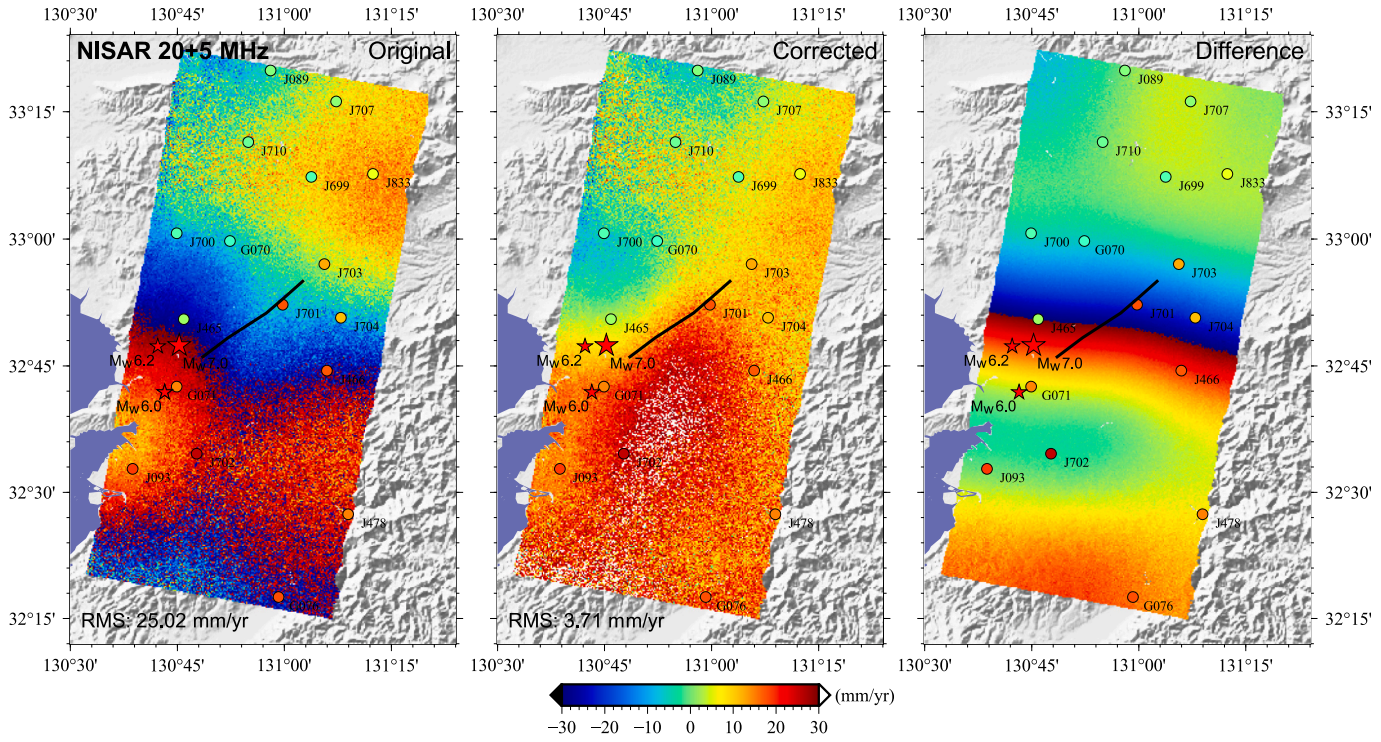

Fig. 15. Azimuth deformation velocity after the 2016 Kumamoto earthquakes in Japan from MAI time series analysis with simulated NISAR 20 + 5 MHz data. GPS stations are represented by circles. The colors inside the circles represent the GPS velocities projected into radar azimuth directions. The thick line in each panel is surface rupture identified from the InSAR coseismic interferogram. The stars denote the epicenters of the foreshocks and mainshock. Note that a much better result is expected with real NISAR data considering NISAR's high duty cycle.

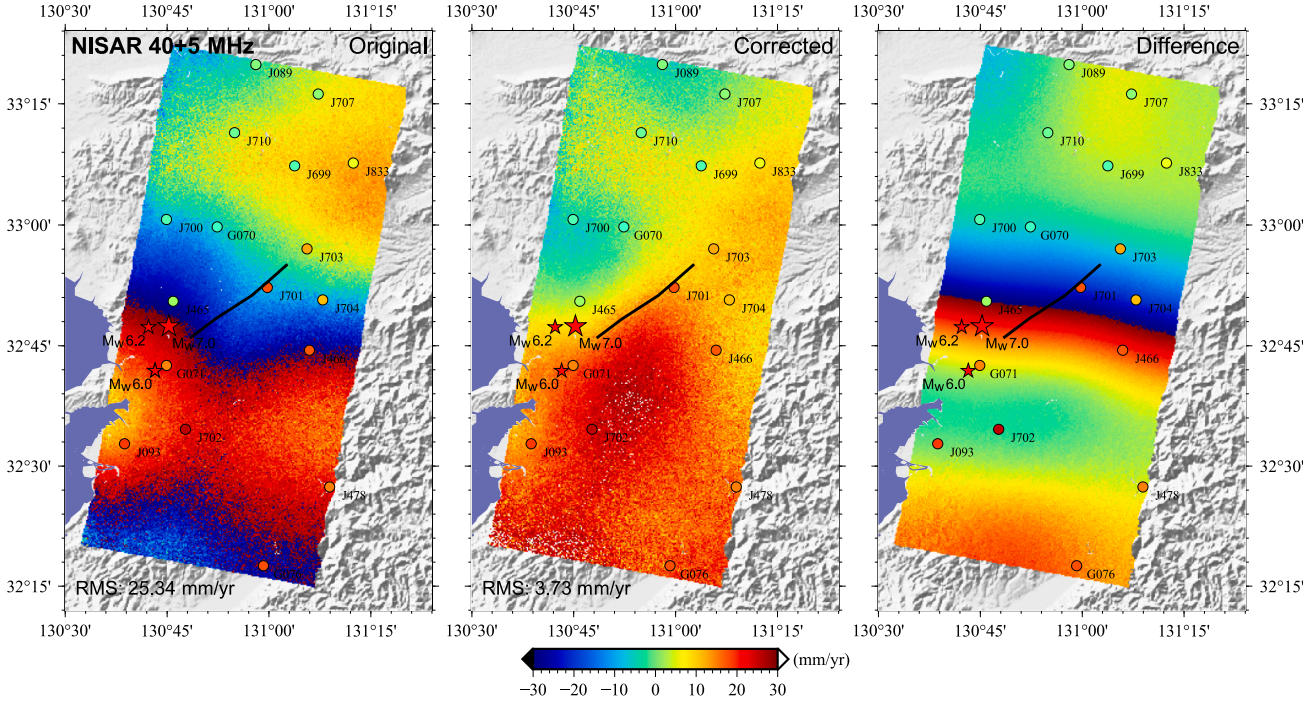

Fig. 16. Azimuth deformation velocity after the 2016 Kumamoto earthquakes in Japan from MAI time series analysis with simulated NISAR 40 + 5 MHz data. GPS stations are represented by circles. The colors inside the circles represent the GPS velocities projected into radar azimuth directions. The thick line in each panel is surface rupture identified from the InSAR coseismic interferogram. The stars denote the epicenters of the foreshocks and mainshock. Note that a much better result is expected with real NISAR data considering NISAR's high duty cycle.

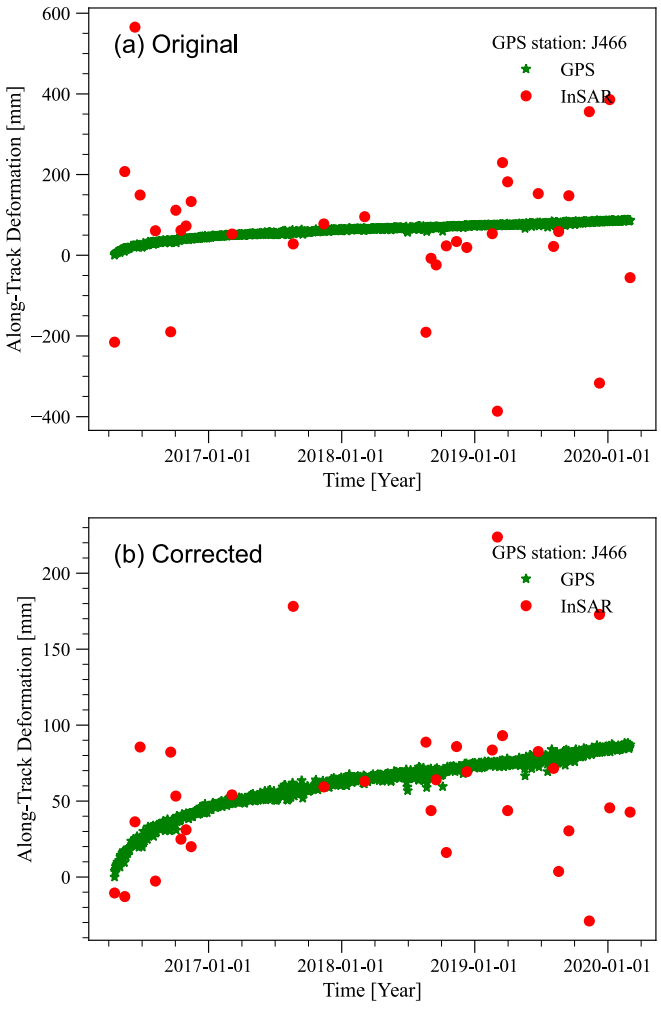

Fig. 17. Azimuth deformation time series at GPS station J466 measured with ALOS-2 84 MHz data.

a proposed observation plan, ROSE-L and Sentinel-1 can provide C-band and L-band data with an acquisition time difference of up to one minute by flying closely, also providing opportunities of improved estimate. For ALOS-4, Japan will be imaged by the 84 MHz stripmap mode 20 times per year on both descending and ascending tracks according to the current version of Basic Observation Scenario (BOS) (JAXA, n.d). 50 % of the global land areas will be imaged by the 28 + 10 MHz mode 9 times per year on ascending tracks.

The resolution of the azimuth measurement is on the order of kilometers, but is still better than that of GPS network as can be seen from Figs. 12–16. Note that Japan is one of the areas that have densest GPS networks in the world. In many applications, the deformation signals are downsampled, often at kilometer resolutions, before used in the geophysical models to save computation (Lohman and Simons, 2001). The azimuth measurements are particularly useful for large faults where deformations are dominated by north-south components, such as the San Andreas Fault in the US, the Main Himalayan Thrust (Wang and Shen, 2020), and the East Anatolian Fault in Türkiye (Weiss et al., 2020). Measuring glacier motion is another potential application. Since many glaciers move fast, further study is required to evaluate the impacts of the ionosphere, and develop robust techniques to estimate ionospheric effects.

5. Conclusions

We have outlined the framework of separating the azimuth motion and ionospheric azimuth shift. We have demonstrated three methods are with highest precisions. Evaluation of the performance of several selected L-band SAR satellites show that, at kilometer resolutions, the azimuth motion measured by MAI can achieve centimeter precision, while the ionospheric azimuth shifts can be estimated with decimeter precision. Based on the evaluation results, we have suggested a strategy for processing azimuth motion and ionospheric azimuth shift. We have presented the time series analysis results of corrected azimuth motions that measure the postseismic deformation of the 2016 Kumamoto earthquakes in Japan. The time series results are expected to be much improved by future missions that have high duty cycles and routinely acquire data on both descending and ascending tracks. Therefore, measuring azimuth motion with future L-band missions would provide a useful azimuth component, even for measuring slow ground motions, which is beneficial to a number of geophysical applications, in particular, those associated with the Earth's tectonic processes.

CRediT authorship contribution statement

Cunren Liang: Writing – review & editing, Writing – original draft, Visualization, Validation, Supervision, Software, Resources, Project administration, Methodology, Investigation, Funding acquisition, Formal analysis, Data curation, Conceptualization. **Eric J. Fielding:** Writing – review & editing, Resources, Project administration, Funding acquisition, Data curation, Conceptualization. **Zhen Liu:** Writing – review & editing, Resources, Investigation, Data curation. **Takeshi Motohka:** Writing – review & editing, Resources, Formal analysis. **Ryo Natsuaki:** Writing – review & editing, Formal analysis. **Sang-Ho Yun:** Writing – review & editing, Formal analysis.

Declaration of competing interest

The authors declare that they have no known competing financial interests or personal relationships that could have appeared to influence the work reported in this paper.

Data availability

Data will be made available on request.

Acknowledgment

This work was supported by National Natural Science Foundation of China under grant 42274026. The ALOS-2 original data are copyright Japan Aerospace Exploration Agency (JAXA) and provided under multiple JAXA PI projects. Some figures were plotted using the GMT software (Wessel et al., 2013). The GPS data were downloaded from Nevada Geodetic Laboratory (http://geodesy.unr.edu/) (Blewitt et al., 2018). We thank Yunjun Zhang, Aerospace Information Research Institute, Chinese Academy of Sciences, for discussions on LuTan-1, as well as the reviewers for helpful comments. Part of this research was carried out at the Jet Propulsion Laboratory, California Institute of Technology, under a contract with the National Aeronautics and Space Administration (80NM0018D0004).

Appendix A. The dispersive nature of the Earth's ionosphere and its effect on SAR imaging

The mechanisms of ionospheric effects on SAR data are already known. Here we explain these mechanisms through our own derivations so that these effects can be presented in a consistent manner and ready for use in further analysis. In particular, we also address their connections to

ionospheric effects on GNSS signals.

Electromagnetic waves propagating in a medium are described by the Maxwell's equations and the constitutive equations. In the Earth's ionosphere, free electrons experience collisions and forces from the electromagnetic field of the waves and the Earth's magnetic field, which satisfies the Lorentz force equation. Ions, on the other hand, can be neglected, as they can hardly be moved by these forces at high frequencies, e.g. microwave frequencies, because they are much more massive than electrons. From these equations and with some assumptions, the complex refractive index of the ionosphere was derived by Appleton (Appleton, 1927; Appleton, 1932), Hartree (Hartree, 1931), Lassen (Lassen, 1927) and Goldstein (Goldstein, 1928). The commonly used form along with its derivation can be found in (Ratcliffe, 1959; Yeh and Liu, 1972; Budden, 1985; Davies, 1990)

$$n^2 = (n_p - i\chi)^2 = 1 - \frac{X}{1 - iZ - \frac{Y_T^2}{2(1-X-iZ)} \pm \left[\frac{Y_T^4}{4(1-X-iZ)^2} + Y_L^2\right]^{1/2}} \tag{A.1}$$

where $i = \sqrt{-1}$, $X = (\omega_N/\omega)^2 = Ne^2/\varepsilon_0 m\omega^2$, $Y = \omega_H/\omega = |e|B/m\omega$, $Y_L = Ycos\theta$, $Y_T = Ysin\theta$, and $Z = \nu/\omega$. In these variables, $\omega = 2\pi f$ and f is the electromagnetic wave frequency (hertz, Hz), $\omega_N = 2\pi f_N$ and f_N is the plasma frequency (hertz, Hz), $\omega_H = 2\pi f_H$ and f_H is the electron gyrofrequency (hertz, Hz), N is the electron number density (per meter^3, m^{-3}), e is the charge on an electron (coulomb, C), ε_0 is the permittivity of free space (farad/m, F/m), m is the rest mass of an electron (kilogram, kg), B is the Earth's magnetic flux density (teslas, T), θ is the angle between the Earth's magnetic field and the electromagnetic wave propagation, and ν is the collision frequency (per second, s^{-1}). The $\pm$ sign means the electromagnetic wave travelling in the ionosphere in the presence of the Earth's magnetic field is split into two characteristic waves whose polarizations do not change as they travel. The equation is called Appleton, Appleton-Hartree or Appleton-Lassen equation or formula. We refer to it as Appleton-Hartree equation hereafter.

The real part of the complex refractive index n_p is the phase refractive index, and the imaginary part χ is the absorption index. The phase of the wave travels at a speed known as phase speed $v_p = c/n_p$, where c is the speed of light in vacuum. The envelope of the wave travels at a speed known as group speed v_g. Similar to phase refractive index n_p, a group refractive index can be defined $n_g = c/v_g$. The phase and group refractive indices are related by the modified Rayleigh equation (Ratcliffe, 1959; Yeh and Liu, 1972; Budden, 1985; Davies, 1990; Hofmann-Wellenhof et al., 2001)

$$n_g = n_p + f\frac{dn_p}{df} \tag{A.2}$$

A medium in which the phase speed varies with wave frequency f is said to be dispersive. For a dispersive medium, it's clear from Eq. (A.2) that the phase and group speeds are different. Dispersion happens when sunlight strikes a dispersive prism, and we see the colors of the rainbow in the prism, because the angle of refraction of each frequency component in the sunlight is related to its phase speed according to Snell's law.

The complete form of refractive index is complex. Collision is usually neglected, so $n \approx n_p$. Various further approximations have been made for practical use (Budden, 1985). Both SAR and GNSS operates in the microwave region of the electromagnetic spectrum. Some of the theoretical and technical development about ionosphere in SAR benefited from the theories and practices in GPS. In GPS, using different methods, the Appleton-Hartree equation is simplified as (Budden, 1985; Leitinger, 1974; Ajayi et al., 1980; Hartmann and Leitinger, 1984; Brunner and Gu, 1991; Bassiri and Hajj, 1993; Hernández-Pajares, 2010; Datta-Barua et al., 2008; Petrie et al., 2011; Moore and Morton, 2011)

$$n_p = 1 - \frac{1}{2}X \pm \frac{1}{2}XYcos\theta - \frac{1}{8}X^2 - \frac{1}{4}XY^2(1 + cos^2\theta) \tag{A.3}$$

Some authors neglect the last one or two terms. Substituting Eq. (A.3) into Eq. (A.2), the group refractive index is obtained

$$n_g = 1 + \frac{1}{2}X \mp XYcos\theta + \frac{3}{8}X^2 + \frac{3}{4}XY^2(1 + cos^2\theta) \tag{A.4}$$

Substituting $X = (\omega_N/\omega)^2 = Ne^2/\varepsilon_0 m\omega^2$, $Y = \omega_H/\omega = |e|B/m\omega$, and $\omega = 2\pi f$ into Eqs. (A.3) and (A.4), the phase and group refractive indices become

$$\begin{aligned} n_p &= 1 - \frac{Ne^2}{2\varepsilon_0 m\omega^2} \pm \frac{N|e^3|Bcos\theta}{2\varepsilon_0 m^2\omega^3} - \frac{N^2e^4}{8\varepsilon_0^2 m^2\omega^4} - \frac{Ne^4B^2}{4\varepsilon_0 m^3\omega^4}(1 + cos^2\theta) = 1 - \frac{Ne^2}{8\pi^2\varepsilon_0 m}\frac{1}{f^2} \pm \frac{N|e^3|Bcos\theta}{16\pi^3\varepsilon_0 m^2}\frac{1}{f^3} - \left[\frac{N^2e^4}{128\pi^4\varepsilon_0^2 m^2} + \frac{Ne^4B^2}{64\pi^4\varepsilon_0 m^3}(1 + cos^2\theta)\right]\frac{1}{f^4} \\ &= 1 - K_2N\frac{1}{f^2} \pm K_3NBcos\theta\frac{1}{f^3} - \left[K_{4,1}N^2 + K_{4,2}NB^2(1 + cos^2\theta)\right]\frac{1}{f^4} \end{aligned} \tag{A.5}$$

$$\begin{aligned} n_g &= 1 + \frac{Ne^2}{8\pi^2\varepsilon_0 m}\frac{1}{f^2} \mp \frac{N|e^3|Bcos\theta}{8\pi^3\varepsilon_0 m^2}\frac{1}{f^3} + \left[\frac{3N^2e^4}{128\pi^4\varepsilon_0^2 m^2} + \frac{3Ne^4B^2}{64\pi^4\varepsilon_0 m^3}(1 + cos^2\theta)\right]\frac{1}{f^4} = 1 + K_{g,2}N\frac{1}{f^2} \mp K_{g,3}NBcos\theta\frac{1}{f^3} + \left[K_{g,4,1}N^2 + K_{g,4,2}NB^2(1 + cos^2\theta)\right]\frac{1}{f^4} \\ &= 1 + K_2N\frac{1}{f^2} \mp 2K_3NBcos\theta\frac{1}{f^3} + \left[3K_{4,1}N^2 + 3K_{4,2}NB^2(1 + cos^2\theta)\right]\frac{1}{f^4} \end{aligned} \tag{A.6}$$

The constants K_1, K_2, $K_{4,1}$ and $K_{4,2}$ can be computed using the values of e, m and ε_0

$$\begin{cases} K_2 = \dfrac{e^2}{8\pi^2\varepsilon_0 m} = 40.31\ \mathrm{m^3/s^2} \\ K_3 = \dfrac{|e^3|}{16\pi^3\varepsilon_0 m^2} = 1.13\times10^{12}\ \mathrm{Am^3/skg} \\ K_{4,1} = \dfrac{e^4}{128\pi^4\varepsilon_0^2 m^2} = 812.38\ \mathrm{m^6/s^4} \\ K_{4,2} = \dfrac{e^4}{64\pi^4\varepsilon_0 m^3} = 1.58\times10^{22}\ \mathrm{A^2m^3/kg^2} \end{cases} \tag{A.7}$$

In some literatures (e.g., Meyer, 2011), $K_2 = 40.28\ \mathrm{m^3/s^2}$, likely due to the use of different e, m and ε_0 values.

The phase of the electromagnetic wave is computed by the integration of phase refractive index along the propagation path. For vacuum, $n_p = n_g = 1$. Assuming the straight path and bended path due to refraction connecting the phase centers of the transmitting and receiving antennas are l_0 and l, respectively, the one-way phase delay in meters is thus given by

$$\begin{aligned} r_p &= \int n_p dl - \int dl_0 \approx \int (n_p - 1) dl_0 = \int \left\{ -K_2 N \frac{1}{f^2} \pm K_3 NB cos\theta \frac{1}{f^3} - \left[K_{4,1} N^2 + K_{4,2} NB^2 (1 + cos^2\theta) \right] \frac{1}{f^4} \right\} dl_0 \\ &= -\frac{K_2}{f^2} \int N dl_0 \pm \frac{K_3}{f^3} \int NB cos\theta dl_0 - \frac{K_{4,1}}{f^4} \int N^2 dl_0 - \frac{K_{4,2}}{f^4} \int NB^2 (1 + cos^2\theta) dl_0 \approx -\frac{K_2}{f^2} \int N dl_0 = -\frac{K_2}{f^2} \mathrm{TEC} \end{aligned} \tag{A.8}$$

where TEC is the total electron content (TEC) along propagation path. In the first approximation, the bending of the propagation path is ignored. The second approximation ignores the high order terms of the electromagnetic wave frequency f. The last line in Eq. (A.8) is the form that is mostly used in SAR analysis. This form accounts for more than 99.9 % of the total ionospheric delays (Hernández-Pajares, 2010). In GPS, this is also the mostly used form, but high order terms were also considered in recent years (e.g., Bassiri and Hajj, 1993; Hernández-Pajares, 2010; Datta-Barua et al., 2008).

Similarly, the one-way group delay in meters is given by

$$\begin{aligned} r_g &= \int n_g dl - \int dl_0 \approx \int (n_g - 1) dl_0 = \int \left\{ K_2 N \frac{1}{f^2} \mp 2K_3 NB cos\theta \frac{1}{f^3} + \left[3K_{4,1} N^2 + 3K_{4,2} NB^2 (1 + cos^2\theta) \right] \frac{1}{f^4} \right\} dl_0 \\ &= \frac{K_2}{f^2} \int N dl_0 \mp \frac{2K_3}{f^3} \int NB cos\theta dl_0 + \frac{3K_{4,1}}{f^4} \int N^2 dl_0 + \frac{3K_{4,2}}{f^4} \int NB^2 (1 + cos^2\theta) dl_0 \approx \frac{K_2}{f^2} \int N dl_0 = \frac{K_2}{f^2} \mathrm{TEC} \end{aligned} \tag{A.9}$$

The signs of Eqs. (A.8) and (A.9) show that the phase delay r_p is an advance, while the group delay r_g is a delay. In these approximated forms, they are equal in absolute value, but with opposite signs. Therefore, the phase travels faster, but the envelope travels slower, than the speed of light in vacuum.

When the electromagnetic wave propagation is not perpendicular to the Earth's magnetic field ($\theta \neq 90^\circ$), the two characteristic waves become a left-handed elliptically polarized wave (ordinary wave, upper sign in Eqs. (A.1) to (A.6)) and a right-handed elliptically polarized wave (extraordinary wave, lower sign in Eqs. (A.1) to (A.6)), respectively. The phase difference between the two polarizations, using Eq. (A.8), leads to the Faraday rotation. The one-way Faraday rotation, in meters following the previous convention, can be given by (Davies, 1990)

$$r_f = \frac{1}{2}(r_{p,+} - r_{p,-}) = \frac{1}{2}\frac{2K_3}{f^3} \int NB cos\theta dl_0 \approx \frac{K_3}{f^3} B cos\theta \int N dl_0 = \frac{K_3}{f^3} \mathrm{TEC} B cos\theta \tag{A.10}$$

A constant geomagnetic field B is assumed for the approximation in Eq. (A.10). The GPS signal is predominantly right-handed circularly polarized, and therefore many authors in the GPS field use the lower sign and think GPS signal is not subject to Faraday rotation. Others argue that the GPS signal still propagates through the ionosphere as ordinary and extraordinary waves, so both of them should be considered (Moore and Morton, 2011).

The linear change of the phase advance corresponds to the group delay in range. In azimuth, the linear change within the synthetic aperture leads to an azimuth pixel shift. High-order terms of the phase advance leads to defocusing in the SAR images in both directions. The one-way azimuth shift in meters is (Liang and Fielding, 2017)

$$a_g = \frac{v_g}{4\pi K_a} \frac{\partial\left(r_p \frac{2\pi f}{c}\right)}{\partial\eta} = \frac{v_g}{4\pi K_a} \left(-\frac{2\pi K_2}{cf} \right) \frac{\partial \mathrm{TEC}}{\partial\eta} = -\frac{v_g}{2cfK_a} K_2 \frac{\partial \mathrm{TEC}}{\partial\eta} \tag{A.11}$$

where η is the azimuth time, v_g is the velocity of the zero Doppler line along the Earth's surface, and K_a ($K_a > 0$) is the azimuth frequency modulation (FM) rate, and is given by (Cumming and Wong, 2005)

$$K_a = \frac{2v_r^2 cos^3\theta_{r,c}}{\lambda R_0} \tag{A.12}$$

where v_r is the effective radar velocity, λ is the radar wavelength, $\theta_{r,c}$ is the squint angle in the rectilinear geometry, and R_0 is the range of closest approach. Substituting Eq. (A.12) into Eq. (A.11), the one-way azimuth shift in meters is given by

$$a_g = -\frac{1}{f^2} \cdot \frac{v_g R_0}{4v_r^2 cos^3\theta_{r,c}} \cdot K_2 \cdot \frac{\partial \mathrm{TEC}}{\partial\eta} \tag{A.13}$$

For future reference, the ionospheric effects in SAR are summarized here. The quantities are evaluated at the radar center frequency $f = f_0$. The two-way phase advance in radians is

$$\phi_{\text{ion}} = r_p \frac{4\pi f}{c}\bigg|_{f=f_0} = -\frac{4\pi K_2}{c f_0}\text{TEC} \tag{A.14}$$

The two-way range shift in meters is

$$r_{\text{ion}} = 2r_g\big|_{f=f_0} = \frac{2K_2}{f_0^2}\text{TEC} \tag{A.15}$$

The two-way azimuth shift in meters is

$$a_{\text{ion}} = 2a_g\big|_{f=f_0} = -\frac{v_g}{c f_0 K_a} K_2 \frac{\partial \text{TEC}}{\partial \eta} = -\frac{1}{f_0^2}\cdot\frac{v_g R_0}{2v_r^2 cos^3\theta_{r,c}}\cdot K_2 \cdot \frac{\partial \text{TEC}}{\partial \eta} \tag{A.16}$$

The one-way Faraday rotation in radians is

$$\Omega_{\text{ion}} = r_f \frac{2\pi f}{c}\bigg|_{f=f_0} = \frac{2\pi K_3}{c f_0^2}\text{TEC} B cos\theta \tag{A.17}$$

Spatial inhomogeneity of the ionosphere leads to the variations of these effects over an image, while temporal variations of the ionosphere lead to the differences of these effects between images acquired at different times. An InSAR pair consists of two acquisitions, and therefore the variables in Eqs. (A.14) to (A.16) ϕ_{ion}, r_{ion}, a_{ion} and TEC should be replaced with $\Delta\phi_{\text{ion}}$, Δr_{ion}, Δa_{ion} and ΔTEC, respectively. In these equations, $K_2 = 40.31\ \text{m}^3/\text{s}^2$, $K_3 = 1.13 \times 10^{12}\ \text{Am}^3/\text{skg}$, TEC is the total electron content along propagation path, B is the Earth's magnetic flux density, θ is the angle between the Earth's magnetic field and the electromagnetic wave propagation, c is the speed of light in vacuum, f_0 is radar center frequency, v_g is the velocity of the zero Doppler line along the Earth's surface, K_a ($K_a > 0$) is the azimuth frequency modulation rate, v_r is the effective radar velocity, $\theta_{r,c}$ is the squint angle in the rectilinear geometry, R_0 is the range of closest approach, and η is the azimuth time.

References

Ajayi, G.O., Hedberg, A., Hamberg, G., 1980. Accurate determination of ionospheric effects on satellite-based positioning systems in terms of residual range error. Radio Sci. 15, 1009–1016.

Appleton, E.V., 1927. The Influence of the Earth's Magnetic Field on Wireless Transmission. URSI Assembly.

Appleton, E.V., 1932. Wireless studies of the ionosphere. J. Inst. Elect. Eng. 71, 642–650.

Bamler, R., 2000. Interferometric stereo radargrammetry: Absolute height determination from ERS-ENVISAT interferograms. In: 2000 IEEE International Geoscience and Remote Sensing Symposium, pp. 742–745.

Bamler, R., Eineder, M., 2005. Accuracy of differential shift estimation by correlation and split-bandwidth interferometry for wideband and delta-k SAR systems. IEEE Geosci. Remote Sens. Lett. 2, 151–155.

Bassiri, S., Hajj, G.A., 1993. Higher-order ionospheric effects on the global positioning system observables and means of modeling them. Manuscr Geodaet 18, 280–289.

Bechor, N.B.D., Zebker, H.A., 2006. Measuring two-dimensional movements using a single InSAR pair. Geophys. Res. Lett. 33, L16311.

Blewitt, G., Hammond, W.C., Kreemer, C., 2018. Harnessing the GPS Data Explosion for Interdisciplinary Science. Eos 99.

Brcic, R., Parizzi, A., Eineder, M., Bamler, R., Meyer, F., 2010. Estimation and compensation of ionospheric delay for SAR interferometry. In: 2010 IEEE International Geoscience and Remote Sensing Symposium, pp. 2908–2911.

Brunner, F.K., Gu, M., 1991. An improved model for the dual frequency ionospheric correction of GPS observations. Manuscr Geodaet 16, 205–214.

Budden, K.G., 1985. The Propagation of Radio Waves: The Theory of Radio Waves of Low Power in the Ionosphere and Magnetosphere. Cambridge University Press, Cambridge, UK p74, p131, p94, p99.

Chen, C.W., 2004. Mitigation of tropospheric InSAR phase artifacts through differential multisquint processing. In: 2004 IEEE International Geoscience and Remote Sensing Symposium, pp. 485–488.

Chen, C.W., Zebker, H.A., 2001. Two-dimensional phase unwrapping with use of statistical models for cost functions in nonlinear optimization. J. Opt. Soc. Am. A 18, 338–351.

Cumming, I.G., Wong, F.H., 2005. Digital Processing of Synthetic Aperture Radar Data: Algorithms and Implementation. Artech House, Norwood, MA, USA.

Datta-Barua, S., Walter, T., Blanch, J., Enge, P., 2008. Bounding higher-order ionosphere errors for the dual-frequency GPS user. Radio Sci. 43, RS5010.

Davies, K., 1990. Ionospheric Radio. The Institution of Engineering and Technology, London, UK p73, p13, p275.

Freeman, A., 2004. Calibration of linearly polarized Polarimetric SAR data subject to faraday rotation. IEEE Trans. Geosci. Remote Sens. 42, 1617–1624.

Freeman, A., Zink, M., Caro, E., Moreira, A., Veilleux, L., Werner, M., 2019. The legacy of the SIR-C/X-SAR radar system: 25 years on. Remote Sens. Environ. 231, 111255.

Goldstein, R.M., Werner, C.L., 1998. Radar interferogram filtering for geophysical applications. Geophys. Res. Lett. 25, 4035–4038.

Goldstein, S., 1928. The influence of the earth's magnetic field on electric transmission in the upper atmosphere. Proceed. Roy. Soc. A: Math. Phys. Eng. Sci. 121, 260–285.

Gomba, G., Parizzi, A., De Zan, F., Eineder, M., Bamler, R., 2016. Toward operational compensation of ionospheric effects in SAR interferograms: the split-spectrum method. IEEE Trans. Geosci. Remote Sens. 54, 1446–1461.

Gondi, F.G., Eppler, J., Caves, R., 2023. Enabling 3D Deformation Monitoring with the CHORUS SAR Constellation. Fringe 2023.

Gray, A.L., Mattar, K.E., Sofko, G., 2000. Influence of ionospheric electron density fluctuations on satellite radar interferometry. Geophys. Res. Lett. 27, 1451–1454.

Hartmann, G.K., Leitinger, R., 1984. Range errors due to ionospheric and tropospheric effects for signal frequencies above 100 MHz. Bull. Géod. 58, 109–136.

Hartree, D.R., 1931. The propagation of electromagnetic waves in a refracting medium in a magnetic field. Math. Proc. Camb. Philos. Soc. 27, 143–162.

Hensley, S., Chen, C., Michel, T., Jones, C., Chapman, B., Muellerschoen, R., 2011. Overview and applications of UAVSAR's multi-squint polarimetric imaging mode. In: 5th International Workshop on Science and Applications of SAR Polarimetry and Polarimetric Interferometry.

Hernández-Pajares, M., 2010. IERS Technical Note No. 36, Chapter 9: Models for Atmospheric Propagation Delays.

Hofmann-Wellenhof, B., Lichtenegger, H., Collins, J., 2001. Global Positioning System: Theory and Practice, (Fifth revised edition. Springer-Verlag Wien GmbH, p. 98.

Hu, J., Li, Z.W., Ding, X.L., Zhu, J.J., Zhang, L., Sun, Q., 2012. 3D coseismic displacement of 2010 Darfield, New Zealand earthquake estimated from multi-aperture InSAR and D-InSAR measurements. J. Geod. 86, 1029–1041.

JAXA. ALOS-4 PALSAR-3 Basic Observation Scenario. https://www.eorc.jaxa.jp/ALOS/en/alos-4/pdf/FTR-210002A_ALOS4PALSAR3_BasicObservationScenario_e.pdf [accessed September 19, 2023].

Jung, H.-S., Won, J.-S., Kim, S.-W., 2009. An improvement of the performance of multiple-aperture SAR interferometry (MAI). IEEE Trans. Geosci. Remote Sens. 47, 2859–2869.

Lassen, H., 1927. Über den einfluss des erdmagnetfeldes auf die fortpflanzung der elektrischen wellen der drahtlosen telegraphie in der atmosphäre. Elektrische Nachricht-Tech. 4, 324–334.

Lavalle, M., Rosen, P., Davidson, M., Horst, S., Tymofyeyeva, K., Oveisgharan, S., Seker, I., Loria, E., Joshil, S., Ahmed, R., 2023. Co-Fliers Mission Concepts for NISAR and ROSE-L to Address Emerging Measurements Needs in Earth Science. Fringe 2023.

Le Vine, D.M., Abraham, S., 2002. The effect of the ionosphere on remote sensing of sea surface salinity from space: absorption and emission at L band. IEEE Trans. Geosci. Remote Sens. 40, 771–782.

Leitinger, R., 1974. Der Einfluss ionosphärischer Ausbreitungsfehler beider geodätischen Anwendung von Navigationssatelliten. Kleinheub. Berich. 17, 321–332.

Liang, C., Fielding, E.J., 2017. Measuring azimuth deformation with L-band ALOS-2 ScanSAR interferometry. IEEE Trans. Geosci. Remote Sens. 55, 2725–2738.

Liang, C., Liu, Z., Fielding, E.J., Bürgmann, R., 2018. InSAR time series analysis of L-band wide-swath SAR data acquired by ALOS-2. IEEE Trans. Geosci. Remote Sens. 56, 4492–4506.

Liang, C., Fielding, E.J., Simons, M., Liu, Z., Bürgmann, R., Zheng, Y., Yun, S.-H., Hubbard, J., 2021. Getting ready for L-band wide-swath InSAR era: Practices and experiences from JAXA ALOS-2 satellite. In: AGU 2021 Fall Meeting.

Liang, C., Fielding, E.J., Liu, Z., Yun, S.-H., Motohka, T., Natsuaki, R., 2022. The potential of L-band SAR satellites for measuring north-south deformation. In: The Joint PI Meeting of JAXA Earth Observation Missions. FY2022.
Lohman, R.B., Simons, M., 2001. Some thoughts on the use of InSAR data to constrain models of surface deformation: noise structure and data downsampling. Geochem. Geophys. Geosyst. 6, Q01007.
López-Dekker, P., Rott, H., Prats-Iraola, P., Chapron, B., Scipal, K., De Witte, E., 2019. Harmony: An Earth explorer 10 mission candidate to observe land, ice, and ocean surface dynamics. In: 2019 IEEE International Geoscience and Remote Sensing Symposium, pp. 8381–8384.
Mao, W., Wang, X., Liu, G., Zhang, R., Shi, Y., Pirasteh, S., 2022. Estimation and compensation of ionospheric phase delay for multi-aperture InSAR: an azimuth split-spectrum interferometry approach. IEEE Trans. Geosci. Remote Sens. 60, 1–14.
Mao, W., Wang, X., Liu, G., Ma, P., Zhang, R., Ma, Z., Tang, J., Lin, H., 2023. Ionospheric phase delay correction for time series multiple-aperture InSAR constrained by polynomial deformation model. IEEE Geosci. Remote Sens. Lett. 20, 4006605.
Meyer, F.J., 2011. Performance requirements for ionospheric correction of low-frequency SAR data. IEEE Trans. Geosci. Remote Sens. 49, 3694–3702.
Michel, R., Avouac, J.-P., Taboury, J., 1999. Measuring ground displacements from SAR amplitude images: application to the landers earthquake. Geophys. Res. Lett. 26, 875–878.
Moore, R.C., Morton, Y.T., 2011. Magneto-ionic polarization and GPS signal propagation through the ionosphere. Radio Sci. 46, RS1008.
Perna, S., Longo, F., Zoffoli, S., Davidson, M., Iannini, L., Lanari, R., 2024. A conceptual performance study on a two-look ScanSAR mode configuration for the forthcoming ROSE-L mission. IEEE Trans. Geosci. Remote Sens. 62, 5201618.
Petrie, E.J., Hernández-Pajares, M., Spalla, P., Moore, P., King, M.A., 2011. A review of higher order ionospheric refraction effects on dual frequency GPS. Surv. Geophys. 32, 197–253.
Quegan, S., Lomas, M.R., 2015. The impact of system effects on estimates of faraday rotation from synthetic aperture radar measurements. IEEE Trans. Geosci. Remote Sens. 53, 4284–4298.
Ratcliffe, J.A., 1959. The Magneto-Ionic Theory & its Applications to the Ionosphere. Cambridge University Press, Cambridge, UK p19, p103.
Raucoules, D., de Michele, M., 2010. Assessing ionospheric influence on L-band SAR data: implications on coseismic displacement measurements of the 2008 Sichuan earthquake. IEEE Geosci. Remote Sens. Lett. 7, 286–290.
Reichle, D.E., 2023. The Global Carbon Cycle and Climate Change, Chapter 10 - the Global Carbon Cycle and the Biosphere. Elsevier.
Rodriguez, E., Martin, J.M., 1992. Theory and design of interferometric synthetic aperture radars. IEE Proc. F-Radar Signal Proc. 139, 147–159.
Rogers, N.C., Quegan, S., 2014. The accuracy of faraday rotation estimation in satellite synthetic aperture radar images. IEEE Trans. Geosci. Remote Sens. 52, 4799–4807.
Rosen, P.A., Hensley, S., Chen, C., 2010. Measurement and mitigation of the ionosphere in L-Band interferometric SAR data. In: IEEE Radar Conference, pp. 1459–1463.
Spencer, M., Ulaby, F., 2016. Spectrum issues faced by active remote sensing: radio frequency interference and operational restrictions. IEEE Geosci. Remote Sens. Magaz. 4, 40–45.
Villano, M., Krieger, G., Moreira, A., 2014. Staggered SAR: high-resolution wide-swath imaging by continuous PRI variation. IEEE Trans. Geosci. Remote Sens. 52, 4462–4479.
Wang, M., Shen, Z.-K., 2020. Present-day crustal deformation of continental China derived from GPS and its tectonic implications. J. Geophys. Res. Solid Earth 125, e2019JB018774.
Wegmüller, U., Werner, C., Strozzi, T., Wiesmann, A., 2007. Ionospheric electron concentration effects on SAR and INSAR. In: 2007 IEEE International Geoscience and Remote Sensing Symposium, pp. 3714–3717.
Wegmüller, U., Werner, C., Frey, O., Magnard, C., Strozzi, T., 2018. Reformulating the split-spectrum method to facilitate the estimation and compensation of the ionospheric phase in SAR interferograms. Proc. Comp. Sci. 138, 318–325.
Weiss, J.R., Walters, R.J., Morishita, Y., Wright, T.J., Lazecky, M., Wang, H., Hussain, E., Hooper, A.J., Elliott, J.R., Rollins, C., Yu, C., González, P.J., Spaans, K., Li, Z., Parsons, B., 2020. High-resolution surface velocities and strain for Anatolia from Sentinel-1 InSAR and GNSS data. Geophys. Res. Lett. 47, e2020GL087376.
Wessel, P., Smith, W.H.F., Scharroo, R., Luis, J., Wobbe, F., 2013. Generic mapping tools: improved version released. Trans. Am. Geophys. Union 94, 409–410.
Wortham, C.B., 2014. Vector Deformation Time-Series from Spaceborne Motion Compensation InSAR Processors. PhD thesis. Stanford University.
Wright, P.A., Quegan, S., Wheadon, N.S., Hall, C.D., 2003. Faraday rotation effects on L-band spaceborne SAR data. IEEE Trans. Geosci. Remote Sens. 41, 2735–2744.
Yamashita, T., Morishita, Y., Kobayashi, T., 2022. Mitigation of ionospheric noise in azimuth offset based on the split-spectrum method. IEEE Trans. Geosci. Remote Sens. 60, 1–11.
Yeh, K.C., Liu, C.H., 1972. Theory of Ionospheric Waves. Academic Press, Inc., New York, NY, USA p183, p280.
Zebker, H.A., 2021. A signal model for PRF dithering in wide-swath, fine-resolution InSAR. IEEE Geosci. Remote Sens. Lett. 18, 1214–1218.